

AN ANALYSIS OF THE GRAIN REFINEMENT OF MAGNESIUM BY ZIRCONIUM

by

PARTHA SAHA

A DISSERTATION

Submitted in partial fulfillment of the requirements  
for the degree of Doctor of Philosophy  
in the Department of Metallurgical and Materials  
Engineering in the Graduate School of  
The University of Alabama

TUSCALOOSA, ALABAMA

2010

Copyright Partha Saha 2010  
ALL RIGHTS RESERVED

## ABSTRACT

A Design of Experiments (DOE) approach was used to conduct a systematic study of the grain refinement of magnesium by zirconium; variables included the amount of zirconium, the pouring temperature, and the settling time prior to casting. Samples were poured into a special “hockey puck” mold designed to reproduce the conditions in permanent mold casting. Optical and scanning electron microscopy (SEM) was utilized to measure the grain size in the final microstructure. Sample dissolution followed by SEM was used to characterize zirconium particle size and morphology both in the master alloy and grain refined samples, while an AccuSizer 770 Photozone/Light Obscuration instrument was used to measure total particle size distributions in the master alloy and grain refined samples. Transmission Electron Microscopy (TEM) was used to identify particles that likely act as suitable heterogeneous nucleation sites for grain refinement. The TEM results show that a range of particle sizes are likely substrates and that only zirconium particles which are faceted are likely nucleation sites. It is apparent that only 1 to 3% of the total particles serve as nucleation sites, but a comparison of the grain density vs. faceted particle density shows close agreement. Equal Channel Angular Extrusion (ECAE) processing of the magnesium-15wt% zirconium master alloy to increase the number of faceted particles resulted in improved grain refinement efficacy. This work suggests that there is a tremendous potential to engineer a more efficient grain refiner.

## DEDICATION

To my family and my beloved wife.

## LIST OF ABBREVIATIONS AND SYMBOLS

$\Delta G_v$  Volume free energy change during solidification

$\gamma$  Interfacial energy

$r^*$  Critical radius of embryo

$\Delta T$  Amount of undercooling

$d$  Dimension of a flat substrate

$\delta$  Interplanar lattice disregistry

$\parallel$  Parallel to

$\wedge$  Angle between two planes

$N_v^P$  Particles density ( $\text{mm}^{-3}$ )

$N_v^G$  Grains density ( $\text{mm}^{-3}$ )

$N_v^F$  Faceted particles density ( $\text{mm}^{-3}$ )

## ACKNOWLEDGMENTS

It gives me immense pleasure to express my deep sense of respect and personal gratitude to my supervisor Dr. Srinath Viswanathan for his excellent guidance and constant encouragement. My sincere appreciation is due for his thoughtful discussion and valuable suggestions. I have been fortunate to work under such co-operative person.

I would especially like to thank my committee members, Dr. G.B. Thompson, Dr. N. Chopra, Prof. Barry J. Andrews, and Prof. R. Batson for their guidance and helpful suggestions to prepare the dissertation.

I am grateful to Mr. Rob Holler, Mr. Johnny Goodwin, and Mr. Rich Martens, and Dr. Mohammad Shamsuzzoha, Central Analytical facilities, The University of Alabama for their constant help to learn and operate the characterization techniques and tools like EPMA, SEM, and TEM. With regards and extreme gratitude I would like to thank Mr. Bob Fanning in the Department of Metallurgical and Materials Engineering for his assistance whenever it was required throughout the PhD program.

I take this opportunity to acknowledge Dr. Sid Bhattacharya, Manager- Geochemical Research laboratory, Department of Geological Sciences, The University of Alabama, for conducting ICP-AES analysis. Ms. Soubantika Palchowdhury, Graduate student in Department of Chemical Engineering for her benign help to prepare the centrifuged samples. Special thanks are due to my friends and colleagues for their support, and installing in me the desire to always do the very best that I can.

In a special way, I would like to thank my dear wife Tamasree Sankar Roy, for all her support she has extended to me, for being my strength and source of inspiration to achieve my dream, my parents and brother for their mental support and encouragement during the course of this work. Without their love, support and encouragement, this would not have been possible.

Finally, I would to like thank United States Automotive Materials Partnerships (USAMP), Department of Energy (DOE), and The University of Alabama for the financial support I got during the PhD program.

## CONTENTS

ABSTRACT .....	ii
DEDICATION .....	iii
LIST OF ABBREVIATIONS AND SYMBOLS .....	iv
ACKNOWLEDGMENTS .....	v
LIST OF TABLES .....	x
LIST OF FIGURES .....	xi
1. PROBLEM STATEMENT .....	1
2. TECHNICAL BACKGROUND .....	3
2.1 Grain Refinement Theories .....	3
2.1.1. Nucleant Particle Theory .....	3
2.1.2. Peritectic Theory .....	4
2.1.3. Solute Theory .....	4
2.2 Nucleation and Growth Mechanisms .....	4
2.3 Homogeneous Nucleation .....	5
2.4 Heterogeneous Nucleation .....	6
2.4.1 Relationship of Critical Undercooling ( $\Delta T$ ) with Particle Size ( $d^*$ ) .....	8
2.4.2 Turnbull's Patch Nucleation Theory .....	9
2.4.3 Adsorption Model .....	10
2.4.4 Other Models .....	11
2.5 Grain Initiation .....	11

2.5.1 Effect of Constitutional Supercooling .....	11
2.5.2 Growth Restriction Factor.....	12
2.5.3 Free Growth Model.....	14
2.6 Grain Refinement of Magnesium by Zirconium.....	15
3. OBJECTIVE, APPROACH, AND TASKS.....	18
Task 1 – DOE Study to Investigate the Effect of Zirconium Addition, Pouring Temperature, and Settling Time on the Resultant Grain Size.....	18
1.1 – DOE Matrix Based on the Magnesium-Zirconium Phase Diagram .....	19
1.2 – Experimental Set-up.....	19
1.3 – Analysis of Settling Behavior of Zirconium Particles .....	19
1.4 – Effect of Zirconium Addition, Pouring Temperature and Settling Time on the Final Microstructure.....	19
Task 2 – TEM Study of Grain Refined Samples .....	20
Task 3 – Analysis of Size, Shape, and Distribution of Zirconium Particles.....	20
3.1 – Dissolution of Grain Refined Samples .....	20
3.2 – Characterization of Dissolution Samples.....	20
3.3 – Comparison of Grain Density with Faceted Particle Density .....	20
Task 4 – Engineer a More Efficient Zirconium-based Grain Refiner for Magnesium Alloys .....	21
4.1 – ECAE Processing of Original Magnesium -15wt% Zirconium Master Alloy .....	21
4.2 – Characterization of the ECAE Processed and Original Master Alloys.....	21
4.3 – Grain Refinement Tests with ECAE Processed Master Alloy.....	21
4. DESIGN OF EXPERIMENTS (DOE) STUDY .....	22

4.1	DOE Matrix Based on the Magnesium-Zirconium Phase Diagram .....	22
4.2	Experimental Set-up.....	23
4.3	Analysis of Settling Behavior of Zirconium Particles .....	24
4.4	Results and Discussion .....	27
4.5	Effect of Zirconium Addition, Pouring Temperature, and Settling Time on the Final Microstructure.....	29
4.6	Conclusion .....	34
5.	TRANSMISSION ELECTRON MICROSCOPY (TEM) STUDY OF PARTICLE SIZE, AND ORIENTATION.....	35
5.1	Introduction .....	35
5.2	TEM Study of Grain Refined Samples .....	36
5.3	Results and Discussion .....	37
5.4	Conclusion .....	48
6.	DISSOLUTION STUDY: PARTICLE MORPHOLOGY, AND SIZE DISTRIBUTION ..	49
6.1	Introduction.....	49
6.2	Particle Size and Morphology.....	51
	6.2.1 Measurement of Particle Size and Distribution .....	52
	6.2.2 Measurement of Faceted Particle Density .....	52
6.3	Results of Particle Size Distributions of Grain Refined Samples.....	53
6.4	Nucleant Particle Efficiency .....	55
6.5	Grain Density vs. Faceted Particles Density.....	57
6.6	Conclusion .....	59
7.	ENGINEERING A MORE EFFICIENT ZIRCONIUM-BASED GRAIN REFINER.....	61

7.1	Introduction.....	61
7.2	ECAE Process.....	62
7.3	ECAE Processing of the Original Magnesium-15 wt% Zirconium Master Alloy.....	63
7.4	Microstructural Characterization of the ECAE Processed Billet.....	64
7.5	Dissolution Study of the ECAE Processed and the Original Master Alloys .....	65
	7.5.1 Particle Size Distribution of the ECAE Processed and the Original Master Alloys....	66
	7.5.2 Faceted Particles in the ECAE Processed and Original Master Alloy.....	67
7.6	Grain Refinement Experiments with ECAE Processed Master Alloy.....	69
8.	CONCLUSION.....	72
	REFERENCES .....	74
	APPENDIX.....	80
	A.1. Grinding and Polishing Procedures for Pure Magnesium and its Alloys .....	80
	A.2. Grain Size Measurement Method Following ASTM Standard E112-96.....	81

## LIST OF TABLES

4.1	Experimental DOE matrix .....	22
5.1	Calculation of planar lattice disregistry and orientation relationship between zirconium nucleus and magnesium matrix for different grain refined samples.....	47
6.1	Particle size distributions (%) in the 0.25 wt% and 1 wt% grain refined samples .....	55
6.2	Comparison of nucleation efficiency of total zirconium particles in different grain refined samples .....	56
6.3	Fraction of faceted zirconium particles present in different grain refined samples.....	58
6.4	Comparison of nucleation efficiency of faceted zirconium particles in different grain refined samples .....	58
7.1	Particle size distributions for the original and ECAE processed master alloys.....	67

## LIST OF FIGURES

2.1	Free energy change for cluster formation as a function of cluster size. ....	5
2.2	A hypothetical spherical cap embryo, interfacial energy, $\gamma$ , relationships among a nucleant (N), a spherical cap solid (S), and the liquid (L) [7]. ....	7
2.3	The interfacial energy, $\gamma$ , relationship among nucleant-solid, nucleant-liquid, and the liquid-solid interface [7]. ....	8
2.4	Undercooling required for nucleation of magnesium grain as a function of zirconium particle size ( $d$ ) from Eq. (2.16).....	9
2.5	Turnbull's patch nucleation model. For a spherical-cap nucleus to become a transformation nucleus, the linear dimension $d$ of the substrate must exceed $2r^*$ [8].....	10
2.6	Atomic adsorption on substrate surface [9]. ....	10
2.7	Constitutionally supercooled region ahead of growing dendrite and the zone in which nucleation can occur, if nucleant particles are present.....	12
2.8	A representation of the constitutionally supercooled zone in front of a growing equiaxed grain assuming that there is no contribution from thermal undercooling or latent heat and negligible thermal gradient exists [15]. ....	13
2.9	Growth of the nucleated solid into the liquid and outward from the face of the substrate involves an increase in curvature of the liquid/solid interface by increase in undercooling. The curvature is maximum when the liquid-solid interface is hemispherical [13]. ....	14
4.1	Magnesium-Zirconium phase diagram showing experimental additions of 0.25, 0.5, and 1wt% zirconium. ....	23
4.2	Hockey puck casting setup used for this work and the mild steel crucible used for the experiments. ....	24
4.3	(a) Scanning electron micrographs showing large zirconium particles and particle clusters along the grain boundary in magnesium-15wt% zirconium used for the work, (b) the enlarged view of the small marked region in (a).....	25

4.4	A schematic diagram showing the mild steel crucible used for the grain refinement experiment. Note: The liquid melt height equivalent to one hockey puck was nearly equal to 20 mm.....	26
4.5	Settling distance for various particle sizes for a settling time of 30 min at (a) 705°C and (b) 815°C, predicted according to Eq. (4.1). .....	26
4.6	Predicted settling behavior of different size of zirconium particles in pure magnesium melt as a function of pouring temperature.....	27
4.7	(a) A schematic drawing of the hockey puck sample from the grain refinement experiments, and (b) location where grain size was measured, i.e. 2 mm from the bottom of the metallographic specimen.....	28
4.8	Optical micrograph in the unetched condition for Mg-0.25 wt% Zr sample poured at 815°C at a settling time of 0 min.....	28
4.9	Optical micrograph in the unetched condition for Mg-0.25 wt% Zr sample poured at 815°C at a settling time of 30 min.....	28
4.10	Optical micrograph of pure magnesium hockey puck sample without any grain refiner addition (magnification 25x).....	29
4.11	Optical micrographs of samples poured at 705°C and a settling time of 0 min for a) 0.25 wt% zirconium, b) 0.5 wt% zirconium, and c) 1 wt% zirconium. The measured grain size is indicated below each micrograph (magnifications 50x). .....	30
4.12	Optical micrographs of samples poured at 705°C and a settling time of 30 min for a) 0.25 wt% zirconium, b) 0.5 wt% zirconium, and c) 1 wt% zirconium. The measured grain size is indicated below each micrograph (magnifications 50x). .....	30
4.13	Optical micrographs of samples poured at 815°C and a settling time of 0 min for a) 0.25 wt% zirconium, b) 0.5 wt% zirconium, and c) 1 wt% zirconium. The measured average grain size is indicated below each micrograph (magnifications 50x). .....	31
4.14	Optical micrographs of samples poured at 815°C and a settling time of 30 min for, a) 0.25 wt% zirconium, b) 0.5 wt% zirconium, and c) 1 wt% zirconium. The measured average grain size is indicated below each micrograph (magnifications 50x). .....	31
4.15	Measured grain size vs. zirconium addition. ....	32
4.16	Measured grain size vs. pouring temperature. ....	32
4.17	Measured grain size vs. settling time.....	33

5.1	(a) Bright field (BF) micrograph of a zirconium precipitate (50 nm) embedded within magnesium matrix, (b) composite selected area diffraction pattern (SADP) of magnesium matrix and the zirconium particle, the particle show a parallel axis orientation relationship with matrix. Electron beam is parallel with $[\bar{1}2\bar{1}3]$ direction. ....	37
5.2	(a) TEM bright field micrograph showing a faceted zirconium particle (equivalent diameter of the particle is 0.23 $\mu\text{m}$ ) embedded in the magnesium matrix, and (b) composite selected area diffraction pattern (SADP) taken with electron beam parallel to $[2\bar{1}\bar{1}0]$ direction from the matrix and the particle.....	38
5.3	(a) Bright field (BF) micrograph of a faceted zirconium particle (equivalent size of 0.5 $\mu\text{m}$ ) found within magnesium matrix, (b) selected area composite diffraction pattern (SADP) of particle and matrix, and (c) of the particle. The particle shows a parallel axis orientation relationship with the matrix.....	39
5.4	(a) Bright field (BF) micrograph of a zirconium particle (length: 1.6 $\mu\text{m}$ and the width: 1 $\mu\text{m}$ ) embedded within magnesium matrix, (b) composite selected area diffraction pattern (SADP) of magnesium matrix and the particle, and (c) HRTEM lattice fringe image at the particle/matrix interface showing continuous lattice fringes. The interplanar spacing for the (0001) plane was measured 0.484 nm and the 0.485 nm in the matrix and particle respectively along the $[2\bar{1}\bar{1}0]$ direction, No dislocation or atomic misfit was observed at the particle/matrix interface suggesting the particle could be a potent nucleation site for the magnesium matrix. ....	40
5.5	(a) Bright field (BF) micrograph of a faceted zirconium particle 4 $\mu\text{m}$ in size embedded within the magnesium matrix, (b) selected area diffraction pattern (SADP) from the matrix, and (c) zirconium particle. The diffraction spots from each pattern were superimposed on each other. A parallel axis orientation relationship exists between the particle and the matrix. The electron beam is parallel with $[\bar{1}2\bar{1}3]$ direction. The intensity of the diffraction spots from the particle was weak due to thickness of the particles. ....	41
5.6	(a) Bright field (BF) micrograph of a zirconium particle (length: 1.4 $\mu\text{m}$ and the width: 0.6 $\mu\text{m}$ ) embedded within magnesium matrix, (b) corresponding selected area diffraction pattern (SADP) of magnesium matrix, and (c) of the zirconium particle. The particle shows a large angle ( $\sim 28^\circ$ ) of misorientation with the matrix. ....	43
5.7	(a) Bright field (BF) micrograph of a 0.15 $\mu\text{m}$ zirconium particle, (b) two different particles of 1 $\mu\text{m}$ and 1.2 $\mu\text{m}$ found at the grain boundaries did not show any orientation relationship with the matrix suggesting that not all the particles selected for grain refinement. The particles were observed in the magnesium-1% zirconium (pouring temperature = 815°C, and settling time = 30 min) grain refined sample.....	43

5.8	(a) Bright field (BF) micrograph of a zirconium particle 0.5 $\mu\text{m}$ size embedded within magnesium matrix, (b) composite selected area diffraction pattern (SADP) of the matrix and the particle show low angle of misorientation between the (11 $\bar{2}$ 2) plane of zirconium and magnesium, Electron beam parallel with $[\bar{1}2\bar{1}3]$ direction (c) HRTEM image showing lattice fringes at the particle-matrix interface. The interplanar spacing was measured 0.257 nm in the matrix and 0.259 nm in the particle for the (10 $\bar{1}$ 1) plane.....	44
5.9	(a) Bright field (BF) micrograph of a zirconium particle of 0.6 $\mu\text{m}$ in size found within magnesium matrix, (b) high resolution TEM image showing lattice fringes at the particle/matrix interface. The interplanar spacing between the fringes was measured 0.320 nm in the matrix and 0.322 nm in the particle for the (0001) plane. Clear atomic misfit was observed at the particle/matrix interface suggesting that the particle was not a likely nucleation site. ....	45
6.1	Particle size distribution of zirconium particles present in magnesium-0.25% zirconium grain refined samples at 0 and 30 min determined using a light obscuration/Photozone method. The drastically lower number of particles at 30 min suggests fading, particle agglomeration and settling with time.....	54
6.2	Particle size distribution of total number of zirconium particles available in magnesium-1.0% zirconium grain refined samples at different settling time determined from light obscuration/photozone method. Total number of particles in the diameter range 0.5-5 $\mu\text{m}$ was calculated as 244,429 and 45,377 in 1 ml of the dissolution sample in 0 min and 30 min sample respectively.....	54
6.3	SEM micrographs of zirconium particles observed from the dissolution study at 0 min (a) magnesium- 0.25 wt% zirconium, (b) magnesium- 1 wt% zirconium; and 30 min (c) magnesium- 0.25 wt% zirconium, (d) magnesium- 1 wt% zirconium grain refined samples. ....	57
6.4	Optical micrographs of samples poured at 705°C at a) 0 min settling time, b) 30 min settling time and (c) 30 min-restirred sample The measured grain size is indicated below of each micrograph (magnifications 50x).....	60
7.1	Optical micrograph in the unetched condition for magnesium-1.0 wt% zirconium sample poured at 815°C, 0 min. ....	61
7.2	SEM micrograph of the magnesium-15wt% zirconium master alloy show zirconium particle and particle clusters greater than 5 $\mu\text{m}$ along the grain boundary. ....	62
7.3	A schematic diagram of the ECAE process. The extrusion direction is illustrated by flow lines 1-1 and 2-2. Deformation is achieved by simple shear along the crossing plane (00) of the channel [37].....	62

7.4	Photograph of magnesium-15 wt% zirconium ECAE processed billet encapsulated in steel can.....	63
7.5	Schematic diagram of the magnesium-15 wt% zirconium ECAE processed billet showing the flow plane or the side plane of the billet, the longitudinal plane the top plane of the billet, the transverse plane, i.e. the plane perpendicular to the long axis of the billet, and the push face of the billet. ....	64
7.6	(a) Scanning electron micrograph showing large zirconium particles and particle clusters along the grain boundary in magnesium-15 wt% zirconium master alloy, (b) enlarged view of the small marked region in (a) showing large particle clusters; (c) Scanning electron micrograph of the ECAE processed magnesium-15wt% zirconium used for the work (d) enlarged view of the small marked region in (a) showing small and large number of zirconium particle. ECAE helped to break up the particle cluster and spread over large volume.....	65
7.7	Particle size distribution of original master alloy and ECAE processed master alloy determined using the light obscuration/photozone method. The total number of particles in the diameter range of 0.5-5 $\mu\text{m}$ was measured to be 383,866 in the original master alloy and 441,055 in the ECAE processed sample.....	66
7.8	SEM micrographs of zirconium particles observed from the dissolution study (a) original master alloy, and (b) ECAE processed master alloy.....	67
7.9	Particle size distribution of faceted zirconium particles observed in the original master alloy and ECAE processed samples.....	68
7.10	Optical micrographs of magnesium-0.1 wt% zirconium sample poured at 815°C 0 min settling time indicate no grain refinement. The measured grain size is indicated below the micrograph (magnifications 50x). ....	69
7.11	Optical micrographs of magnesium-2 wt% zinc sample poured at 815°C, 0 min e indicating no grain refinement. The measured grain size was 476 $\mu\text{m}$ (magnification 50x).....	70
7.12	Optical micrographs of magnesium-2 wt% zinc-0.05 wt% zirconium sample poured at 815°C, 0 min (a) using original master alloy indicate no grain refinement, and (b) using ECAE processed master alloy indicate significant grain refinement. For magnesium-2 wt% zinc-0.1 wt% zirconium sample poured at 815°C, 0 min (c) using original master alloy showing grain refinement and (d) using ECAE processed master alloy showing measurable improvement in grain refinement The measured grain size is indicated below the micrographs (magnification 50x).....	71

## 1. PROBLEM STATEMENT

With the ever increasing demand for weight reduction in automotive parts for better fuel economy, magnesium alloys have attracted considerable interest and research as next-generation structural materials due to their low density, high specific strength and excellent castability [1]. High volumes of near net-shaped components can be produced at relatively low cost using casting processes, particularly for automotive applications. An important requirement for cast alloys is the availability of a suitable grain refiner that can be added to the molten alloy during casting. Grain refinement has several benefits in cast alloys such as uniform microstructure, distribution of second phase and microporosity on a finer scale [2], better feeding to eliminate shrinkage porosity and improved mechanical properties [3]. Finer grains also improve surface finish and impart superior machinability [4].

Zirconium is well known as an excellent grain refiner for magnesium alloyed with zinc, silver, calcium, copper or thorium because these elements are compatible with zirconium and do not poison the grain refining ability of zirconium [5]. Also, zirconium is a heavy element with a density almost four times that of magnesium ( $\rho_{Mg} = 1740 \text{ kg/m}^3$ ,  $\rho_{Zr} = 6520 \text{ kg/m}^3$ ). The addition of zirconium into molten magnesium results in the loss of zirconium by settling, because during melting zirconium particles settle to the bottom of the crucible and are wasted as sludge. In addition, zirconium is expensive and currently approximately 1 wt% zirconium is added to ensure grain refinement.

The goal of this study is to understand the mechanism of grain refinement of magnesium by zirconium and identify the requirements for a more efficient grain refiner. A permanent mold based “hockey puck” experimental setup will be used to quantify the grain refinement efficacy of zirconium in pure magnesium. A Design of Experiments (DOE) approach will be used to conduct a systematic study of the grain refinement behavior of magnesium by zirconium; variables include temperature, settling time and amount of zirconium addition prior to casting.

Optical and scanning electron microscopy (SEM) will be utilized to measure the average grain size in the final microstructure. Transmission electron microscopy (TEM) will be used to explore and establish the orientation relationship between zirconium particles and the parent magnesium matrix. The results from the above tasks will be used to understand the mechanism of grain refinement of magnesium by zirconium and engineer an efficient zirconium-based grain refiner for magnesium alloys.

## 2. TECHNICAL BACKGROUND

Grain refinement is an effective method for control of grain size and morphology during casting. Several methods have been reported to achieve grain refinement in the final microstructure, e.g., inoculation, rapid cooling, electromagnetic or mechanical agitation, ultrasonic cavitation, etc. [6]. However, the most widespread technique of grain refinement is the inoculation of the melt or the introduction of extraneous nucleating agents to a liquid melt. Inoculation yields an equiaxed grain microstructure. The addition of nucleating agents has historically been made as master alloys (hardeners) in the form of shot, rod, waffle, or briquette.

Two major alloys systems that benefit from the excellent grain-refining ability of inoculants are non-aluminum containing magnesium alloys that use zirconium and commercial aluminum alloys inoculated with Al-Ti-B master alloys [5-7].

### 2.1 Grain Refinement Theories

The important theories pertinent to grain refinement have been known for more than fifty years. During this period, numerous models have been proposed to account for grain nucleation and growth process; these are discussed next.

#### 2.1.1. Nucleant Particle Theory

The requirement for nucleating the primary crystals lies in the close lattice mismatch with the nucleating agent and requires very small constitutional undercooling. Particles that show lattice mismatch with the matrix and require low undercooling are likely to be good nucleating agents [8, 9].

### 2.1.2. Peritectic Theory

According to the peritectic theory, particles that are suitable as nucleant particles undergo a peritectic reaction where the nucleant solid ( $\beta$ ) reacts with the liquid and forms the primary  $\alpha$  phase, i.e.



From the above,  $\beta$  would be a suitable nucleant particle. However, this theory was based on the grain refinement behavior of  $\text{TiAl}_3$  in the Al-Ti system. Later it was revealed that better grain refinement could occur by the addition of boron at relatively low titanium levels 0.0 to 0.05 wt% titanium [10]. It is now generally accepted that nucleation occurs on  $\text{TiB}_2$  particles and the peritectic reaction doesn't play a role in grain refinement.

### 2.1.3. Solute Theory

This theory proposes that nucleants in conjunction with segregating solutes influence grain refinement. The solute builds up a constitutional undercooled zone in front of the growing solid-liquid interface. This undercooled zone facilitates nucleation if nucleant particles are present [11].

## 2.2 Nucleation and Growth Mechanisms

Grain nucleation and grain growth are two important mechanisms during solidification. Nucleation is a thermally activated process where the crystallite is formed from the metastable liquid. It is broadly divided into two categories: homogeneous and heterogeneous nucleation.

### 2.3 Homogeneous Nucleation

During homogeneous nucleation, solid forms from the liquid without the involvement of an extraneous surface or site in contact with the melt. The energetics of cluster formation for a spherical geometry can be expressed in terms of interfacial energy and volume free energy contributions as

$$\Delta G(r)_{\text{hom}} = 4\pi r^2 \gamma_{SL} + \frac{4}{3} \pi r^3 \Delta G_v \quad (2.2)$$

where,  $r$  = cluster size

$\Delta G(r)$  = Free energy change to form a cluster of size  $r$

$\gamma_{SL}$  = solid-liquid interfacial energy

$\Delta G_v$  = Volume free energy change during solidification (driving force).

Fig. 2.1 shows the change in free energy as a function of cluster size. From Fig. 2.1, the critical radius,  $r^*$ , of the cluster whose further growth will decrease the free energy of the system, is given by

$$\frac{d\Delta G(r)_{\text{hom}}}{dr} = 8\pi r \gamma_{SL} + 4\pi r^2 \Delta G_v = 0 \quad \text{or} \quad r^* = -\frac{2\gamma_{SL}}{\Delta G_v} \quad (2.3)$$

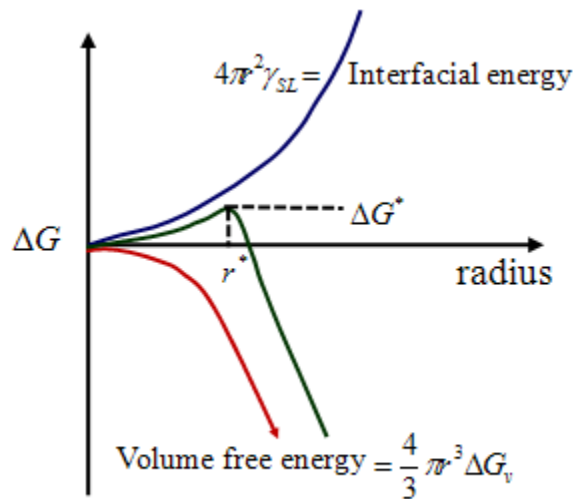


Fig. 2.1 Free energy change for cluster formation as a function of cluster size.

Accordingly,

$$\Delta G_{\text{hom}}^*(r^*) = 4\pi \frac{4\gamma_{SL}^2}{\Delta G_v^2} \gamma_{SL} - \frac{4}{3} \pi \frac{8\gamma_{SL}^3}{\Delta G_v^3} \Delta G_v = \frac{16\pi\gamma_{SL}^3}{3\Delta G_v^2} \quad (2.4)$$

The free energy change on forming a solid from a liquid at the equilibrium transformation temperature,  $T_m$ , can be written as:

$$\Delta G_v = \Delta H - T_m \Delta S = 0 \quad \text{or} \quad \Delta H = T_m \Delta S \quad (2.5)$$

where  $\Delta G_v$  = Gibbs free energy change,  $\Delta H$  = Change in enthalpy, and  $\Delta S$  = Change in entropy.

At a temperature other than  $T_m$ ,

$$\Delta G_v = \Delta H - T \Delta S \neq 0$$

Substituting for  $\Delta H$  from Eq. 2.4

$$\Delta G_v = T_m \Delta S - T \Delta S \quad \text{or} \quad \Delta G_v = (T_m - T) \Delta S = \Delta T \Delta S = \frac{\Delta H \Delta T}{T_m} \quad (2.6)$$

where  $\Delta T$  is undercooling or the difference between the solidification temperature and the equilibrium liquidus or melting point. Therefore,

$$r_{\text{hom}}^* = -\frac{2\gamma_{SL}}{\Delta G_v} \quad \text{or} \quad -\frac{2\gamma_{SL} T_m}{\Delta H \Delta T} \quad (2.7)$$

Thus, if the radius of solid *embryo* is greater than the critical radius,  $r_{\text{hom}}^*$ , the *embryo* will survive.

From Eq. (2.6),

$$r_{\text{hom}}^* \propto \frac{1}{\Delta T} \quad (2.8)$$

Therefore, the smaller the critical radius, the larger the undercooling required.

## 2.4 Heterogeneous Nucleation

The energetics during heterogeneous nucleation is illustrated schematically in Fig. 2.2.

From Fig. 2.2 the total free energy change during heterogeneous nucleation can be expressed as:

$$\Delta G(r)_{\text{het}} = V_{SC} \Delta G_v + A_{SL} \gamma_{SL} + A_{NS} (\gamma_{NS} - \gamma_{NL}) \quad (2.9)$$

where,  $V_{SC}$  = spherical cap volume, and

$A_{SL}$ ,  $A_{NS}$ ,  $A_{NL}$  are the solid-liquid, nucleant-solid, and the nucleant-liquid interfacial areas.

The surface area of spherical cap,  $A_{SL} = 2\pi rh = 2\pi r^2 (1-\cos\theta)$

The area between the spherical cap and the nucleant,  $A_{NS} = \pi r^2 \sin^2\theta$

The volume of the spherical cap

$$V_{SC} = \frac{\pi h^2 (3r - h)}{3} = \frac{\pi r^2 (1 - \cos\theta)^2 (3r - r + r \cos\theta)}{3} \quad (2.10)$$

$$V_{SC} = \frac{\pi r^3}{3} (2 - 3\cos\theta + \cos^3\theta)$$

From equilibrium, in Fig. 2.3

$$\gamma_{NL} = \gamma_{SL} \cos\theta + \gamma_{NS} \quad \text{or} \quad \cos\theta = \frac{\gamma_{NL} - \gamma_{NS}}{\gamma_{SL}} \quad (2.11)$$

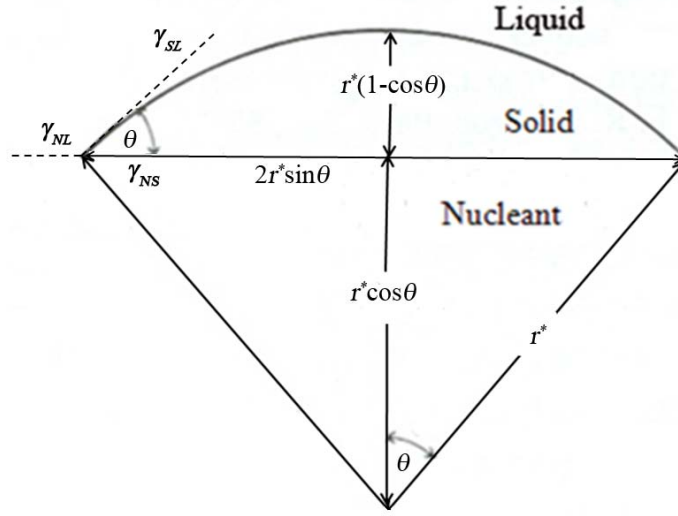


Fig. 2.2 A hypothetical spherical cap embryo, interfacial energy,  $\gamma$ , relationships among a nucleant (N), a spherical cap solid (S), and the liquid (L) [12].

Consequently,  $\Delta G(r)_{het} = V_{SC}\Delta G_v + A_{SL}\gamma_{SL} - A_{NS}\gamma_{SL} \cos\theta$

$$\text{or, } \Delta G(r)_{het} = \frac{1}{3}\pi r^3 (2 - 3\cos\theta + \cos^3\theta)\Delta G_v + 2\pi r^2 (1 - \cos\theta)\gamma_{SL} - \pi r^2 \sin^2\theta \cos\theta \gamma_{SL} \quad (2.12)$$

Rearranging the terms,

$$\Delta G(r)_{het} = \left(\frac{4}{3}\pi r^3 \Delta G_v + 4\pi r^2 \gamma_{SL}\right) \left(\frac{2 - 3\cos\theta + \cos^3\theta}{4}\right)$$

Using Eq. (2.1)

$$\Delta G(r)_{het} = \Delta G(r)_{hom} f(\theta)$$

$$\text{where, } f(\theta) = \frac{1}{4}(2 + \cos\theta)(1 - \cos\theta)^2$$

$$\text{at } r = r^*, \Delta G^*(r^*)_{het} = \Delta G^*(r^*)_{hom} f(\theta)$$

$$\text{or, } \Delta G^*(r^*)_{het} = \frac{16\pi\gamma_{SL}^3}{3\Delta G_v^2} f(\theta)$$

$$\text{so, } r_{hom}^* = -\frac{2\gamma_{SL}}{\Delta G_v} = r_{het}^* \quad \text{and} \quad r_{hom}^* = -\frac{2\gamma_{SL}T_m}{\Delta H\Delta T} = r_{het}^* \quad (2.13)$$

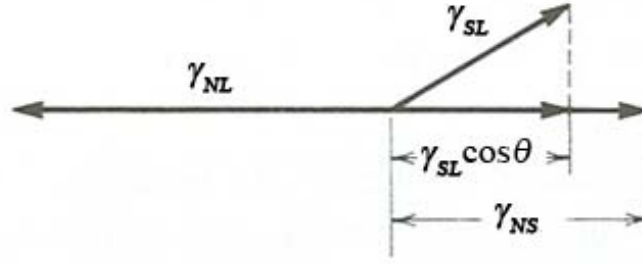


Fig. 2.3 The interfacial energy,  $\gamma$ , relationship among nucleant-solid, nucleant-liquid, and the liquid-solid interface [12].

#### 2.4.1 Relationship of Critical Undercooling ( $\Delta T$ ) with Particle Size ( $d^*$ )

Earlier, the critical radius  $r^*$  for heterogeneous nucleation was calculated as

$$r_{het}^* = -\frac{2\gamma_{SL}}{\Delta G_v} \quad (2.14)$$

where,

$$\Delta G_v = \frac{\Delta H\Delta T}{T_m} \quad (2.15)$$

and  $\Delta T$  is undercooling.

For magnesium the thermodynamic parameters are well known:

$T_m$  = melting point of magnesium = 922.8K,  $\Delta H$  = change in enthalpy during solidification =  $5.898 \times 10^8 \text{ J/m}^3$ , and  $\gamma_{SL} = 115 \times 10^{-3} \text{ J/m}^2$ .

Then

$$r^* (\mu m) = -\frac{0.36}{\Delta T} \quad \text{or} \quad d^* (\mu m) = -\frac{0.72}{\Delta T} \quad (2.16)$$

Fig. 2.4 shows the undercooling required to nucleate a magnesium grain as a function of particle size. Note that a greater undercooling is required for smaller nuclei, suggesting that during solidification larger nuclei will be activated first.

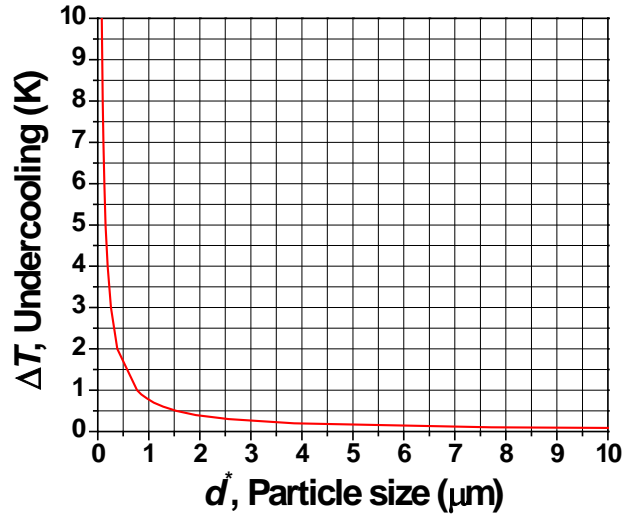


Fig. 2.4 Undercooling required for nucleation of magnesium grain as a function of zirconium particle size ( $d^*$ ) from Eq. (2.16).

#### 2.4.2 Turnbull's Patch Nucleation Theory

Turnbull [13] noted that an embryo of the crystalline phase formed on a patch (i.e., substrate) could become an active transformation nucleus only when the critical nucleus radius  $r^*$  is less than the radius of the patch. In order to be able to accommodate a spherical-cap nucleus, the minimum substrate surface area and dimension ( $d$ ) need to satisfy  $\pi(r^* \sin\theta)^2$  and  $2r^* \sin\theta$ , respectively (see Fig. 2.5). Since  $2r^* \sin\theta < 2r^*$ , in principle a flat substrate or patch with a linear dimension ( $d$ ) in the range  $2r^* \sin\theta < d < 2r^*$  can still act as a nucleating substrate. However, the nucleus thus formed will not be able to grow into a grain. However, when  $d > 2r^*$ , any nucleus formed on the patch surfaces with a radius larger than  $2r^* \sin\theta$  will be able to become a transformation nucleus, i.e., it will grow on the surface to a dimension exceeding  $2r^*$  and thence into the body of the supercooled liquid to become a grain. When  $d < 2r^*$ , a crystal nucleus

formed on the patch surface can still grow to the patch boundary, but will not in general, be able to become a transformation nucleus.

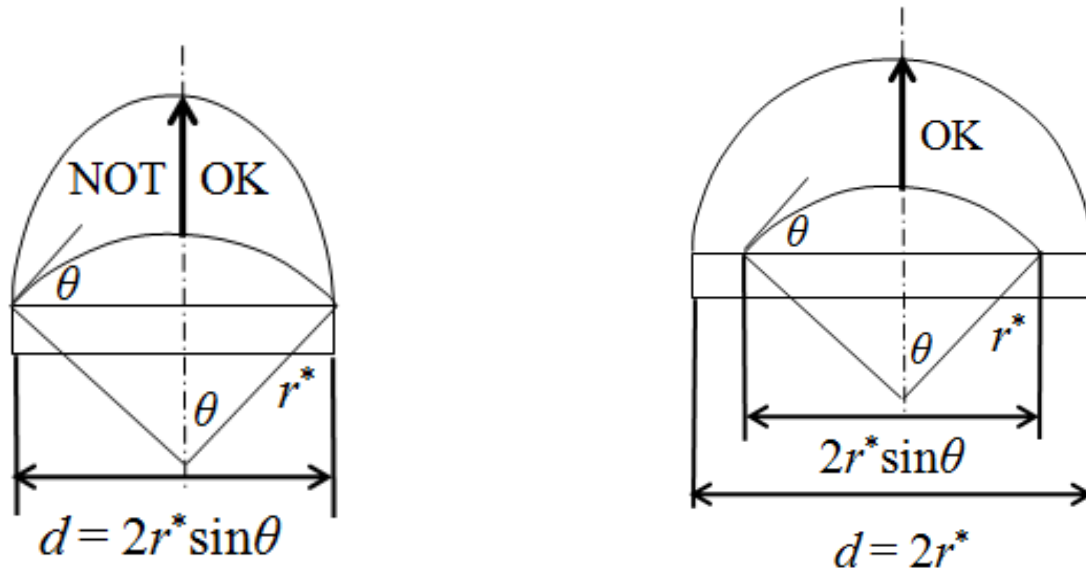


Fig. 2.5 Turnbull's patch nucleation model. For a spherical-cap nucleus to become a transformation nucleus, the linear dimension  $d$  of the substrate must exceed  $2r^*$  [13].

### 2.4.3 Adsorption Model

Sundquist [14] proposed that during heterogeneous nucleation, a nucleus formed at low undercooling and hence low contact angle should be treated as "a monolayer of atoms occupying the atomic sites of the catalyst surface". Accordingly, the atoms in the adsorbed layer should be able to provide the starting point for growth. Later, Cantor [15] provided an adsorption model for heterogeneous nucleation (Fig. 2.6).



Fig. 2.6 Atomic adsorption on substrate surface [14].

#### 2.4.4 Other Models

Maxwell-Hellawell [16] proposed a mechanism that combines the spherical cap model with wetting, for grain formation on faceted substrate particles. They assumed that after a spherical-cap nucleus forms on a facet of a substrate particle, that particle will be immediately enveloped in the matrix due to efficient wetting implied at small undercoolings ( $< 2^{\circ}\text{C}$ ), which also implies a small contact angle ( $\theta$ ). Subsequent growth of the spherical envelope was described as a function of the melt undercooling using a spherical growth model. They also added that at a given cooling rate, the efficiency of a grain refiner not only depends how well the substrate is wet but also on the alloy constitution.

### 2.5 Grain Initiation

Grain formation on a potent nucleant substrate was elucidated by various researchers. Turnbull first hypothesized this in his liquid mercury droplet experiment [17]. The population density of solidified droplets increases stepwise as the amount of undercooling  $\Delta T$  is increased in steps, time independent at a fixed temperature. Maxwell and Hellawell [11] pointed out that initiation of grains stifles further nucleation. Their model was based on soft impingement of thermal diffusion fields around the growing grains. The reason for their assumption was that the thermal diffusion coefficient is orders of magnitude greater than the solute diffusion coefficient.

#### 2.5.1 Effect of Constitutional Supercooling

Constitutional supercooling occurs as solute is rejected at the solid-liquid interface during solidification as shown in Fig. 2.7. During growth, solute rejection builds up a constitutionally

supercooled zone ahead of the interface. This supercooled zone facilitates further nucleation and initiates a new grain if nucleant particles are present.

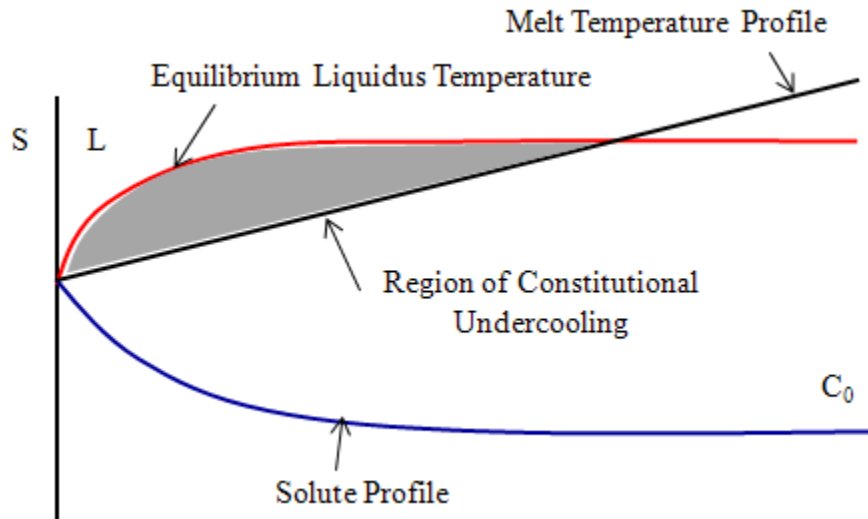


Fig. 2.7 Constitutionally supercooled region ahead of growing dendrite and the zone in which nucleation can occur, if nucleant particles are present.

### 2.5.2 Growth Restriction Factor

Maxwell and Hellawell [11] first considered the growth of spherical crystals restricted by the partitioning of a single solute. They proposed that, to a good approximation, the crystal growth rate for a given supercooling is proportional to the diffusivity of the solute in the liquid and inversely proportional to a parameter  $Q = m(k-1)C_0$ , termed later as a growth restriction parameter by Greer *et al.* [18].

Easton and StJohn [19] showed that the growth restriction term could be derived based on non-equilibrium solidification. They assumed that a constitutional supercooling of  $\Delta T_c$  is required for a nucleation event to occur and that there are sufficient substrates present. Then, nucleation occurs as soon as the constitutional supercooling (see Fig. 2.8) required for nucleation,  $\Delta T_n$  is achieved.

The equilibrium liquidus temperature,  $T_{le}$  and the actual temperature,  $T_{actual}$  are calculated as:

$$m_L = \frac{T_{le} - T_m}{C_o} \quad \text{or} \quad T_{le} = T_m + m_L C_o . \quad (2.17)$$

Similarly, 
$$m_S = \frac{T_{actual} - T_m}{C_S} \quad \text{or} \quad T_{actual} = T_m + m_S C_S . \quad (2.18)$$

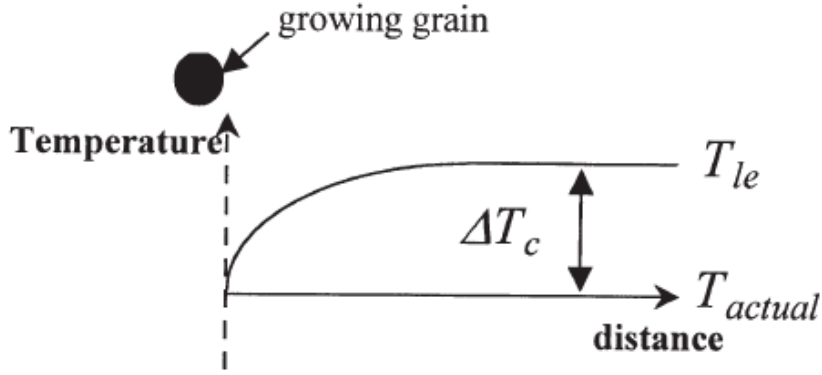


Fig. 2.8 A representation of the constitutionally supercooled zone in front of a growing equiaxed grain assuming that there is no contribution from thermal undercooling or latent heat and negligible thermal gradient exists [15].

The maximum constitutional supercooling,  $\Delta T_C$  can be calculated as

$$\begin{aligned} \Delta T_C &= T_{le} - T_{actual} = T_m + m_L C_o - (T_m + m_S C_S) \\ &= m_L C_o - \frac{m_L C_S}{k} = m_L (C_o - C_L) \end{aligned} \quad (2.19)$$

where, partition coefficient,  $k = \frac{m_L}{m_S} = \frac{C_S}{C_L}$ . (2.20)

When the growth of a single grain is considered, then the amount of constitutional supercooling developed as solidification proceeds can be related to the fraction solid,  $f_s$ , by substituting the

Scheil equation [20]

$$C_L = \frac{C_o}{(1 - f_s)^{1-k}} . \quad (2.21)$$

Therefore, 
$$\Delta T_C = m_L C_o \left( 1 - \frac{1}{(1 - f_s)^{1-k}} \right) \quad (2.22)$$

The initial rate of development of constitutional supercooling is defined by

$$\left. \frac{d\Delta T_C}{df_s} \right|_{f_s=0} = m_L C_o (k - 1) (1 - f_s)^{k-2} \quad (2.23)$$

At  $f_s = 0$ ,  $\frac{d\Delta T_c}{df_s} = m_L C_0 (k - 1)$  which is the growth restriction factor,  $Q$ .

The Growth Restriction Factor (GRF),  $Q$ , is the calculation of the rate of development of the constitutional supercooling zone with respect to fraction solid at zero fraction solid, i.e. the beginning of growth. The strong grain refining ability of zirconium is attributed by many authors [21, 22] to the high growth restriction factor of zirconium in magnesium. The growth restriction factor of zirconium was found to be highest among all the elements that promote grain refinement of magnesium [22].

### 2.5.3 Free Growth Model

Greer *et al.* [18] proposed a model on the experimental evidence they had for the grain refinement of an aluminum alloy by Al-Ti-B grain refiner. They assumed that nucleation occurs on the face of the nucleating substrate at very low undercooling and that the nucleus forms as a low contact angle hemispherical cap shown in Fig. 2.9.

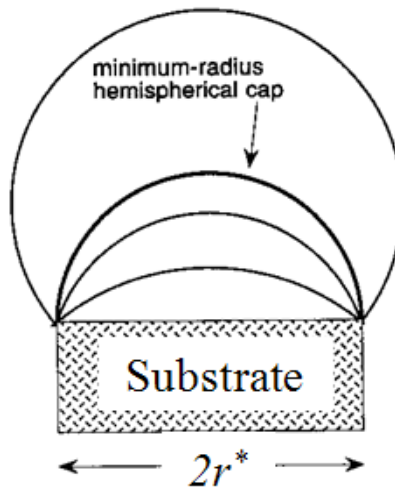


Fig. 2.9 Growth of the nucleated solid into the liquid and outward from the face of the substrate involves an increase in curvature of the liquid/solid interface by increase in undercooling. The curvature is maximum when the liquid-solid interface is hemispherical [18].

They proposed that grain formation is growth limited rather than nucleation limited. The radius of a particle cannot go below the critical value  $r^*$  for nucleation at a given temperature and undercooling. If the diameter of the particle is such that  $d < 2r^*$ , then free growth of the particle is not possible. However, growth becomes possible when the undercooling is increased, thus reducing  $r^*$ . As undercooling is increased, progressively smaller particles become centers for free growth, which occurs as soon as the required undercooling is reached.

## 2.6 Grain Refinement of Magnesium by Zirconium

It is accepted that zirconium satisfies all of the requirements of a good grain refiner required by theory, because:

1. Zirconium and magnesium have the same crystal structure (HCP) and the lattice discrepancy between zirconium and magnesium is very small (Zr:  $a = 0.323$  nm,  $c = 0.514$  nm and Mg:  $a = 0.320$  nm,  $c = 0.520$  nm) [5].
2. A peritectic reaction occurs close to 0.5 wt% zirconium at 654°C. A zirconium-rich phase precipitates from the liquid and reacts with magnesium to form a  $\alpha$ -magnesium phase.
3. Zirconium has highest growth restriction factor among all elements that promote grain refining in magnesium [21, 22].

While zirconium is an effective grain refiner, it suffers from two drawbacks. First, zirconium is an expensive addition. Second, due to limited solubility of zirconium in magnesium an excess of zirconium needs is introduced in order to achieve the optimum grain refinement [23]. The exact mechanism of grain refinement by zirconium is still being debated.

Grain refinement in magnesium alloys is mainly accomplished by magnesium-zirconium master alloys. Due to limited solid solubility of zirconium in magnesium, most of the zirconium

is present as either isolated particles or as particle clusters. Currently, in foundries, approximately 1 wt% zirconium is added to ensure grain refinement. Qian *et al.* [24-26] added 1 wt% zirconium in the form of Zirmax<sup>®</sup> (Mg-33.3 wt% Zr) master alloy to a pure magnesium melt at 730°C and 780°C. In the final microstructure, the undissolved zirconium particles were either found in the form of particles or as large clusters (>10 μm). These clusters did not take part in the grain refinement process and settled to the bottom of the crucible. The settling behavior of zirconium particles is governed by the initial particle size distribution in the master alloy.

The magnesium rich region of the binary Mg-Zr phase diagram (see Fig. 4.1) shows that grain refinement of magnesium can occur in theory by a peritectic reaction at 654°C, where  $\alpha$ -zirconium reacts with liquid and forms a  $\alpha$ -magnesium phase [5]. A recent modification of the magnesium-zirconium phase diagram suggests that the maximum solubility of zirconium is 0.5 wt% at 654°C [27, 28].

Qian *et al.* [24] found zirconium-rich cores, the majority of which are pure zirconium particles, at the center of magnesium grains or at the grain edge. Electron microprobe analysis of these particles showed that the particle sizes were between 1 and 5 μm, suggesting that only particles within this size range acted as nuclei for the grains. Particles which were greater than 5 μm were not associated with zirconium-rich cores.

Qian *et al.* [29-31] reported on the development of a new magnesium-zirconium master alloy (AM-cast) with zirconium particles smaller than 10 μm. They reported that the newly developed master alloy provided excellent grain refinement when added to pure magnesium. The excellent grain refining ability was attributed to the fine size and even distribution of the zirconium particles in the master alloy. Qian *et al.* [32] also demonstrated that the efficiency of a

Zirmax<sup>®</sup> master alloy was improved by hot rolling the master alloy ingots into thin plates. The subsequent improvement in the grain refining behavior was attributed to improved particle size distribution in the rolled master alloy.

Qian *et al.* [29] suggested that grain refinement in magnesium is affected by both soluble and insoluble zirconium in the melt. They suggested that while the majority of grain refinement is achieved from soluble zirconium, insoluble zirconium particles also contribute to the grain refinement. Further, they report that dissolution of zirconium in molten magnesium occurs very quickly in the temperature range of 680–780°C, if the zirconium particles released from the master alloy are brought in contact with the melt by appropriate stirring. By contrast, dissolution of settled particles, which reside at the bottom of the crucible, was sluggish even with stirring [25]. Lee *et al.* [21] observed grain refinement of magnesium at low concentrations of zirconium (0.04 – 0.32 wt %). However, the grain size reached a constant value beyond 0.32 wt% of zirconium. Cao *et al.* [33] used Electron probe microanalysis (EPMA) of the matrix to show that the soluble zirconium content is well below that required for the peritectic reaction, which they suggested was at 0.45 wt% zirconium. Based on this observation, the authors claimed that the peritectic reaction is not a requirement for grain refinement. Note, however, that Cao *et al.* [33] added 1 wt% zirconium to the melt.

### **3. OBJECTIVE, APPROACH, AND TASKS**

This work will identify the nucleation and growth mechanisms during grain refinement and engineer a grain refiner that is more efficient than the current grain refiner. The objectives of the proposed research are to:

1. Experimentally investigate the grain refinement of magnesium by zirconium,
2. Understand and elucidate factors that determine the final grain size, and
3. Engineer a more efficient zirconium based grain refiner for magnesium alloys.

The following tasks were used to accomplish the project objectives.

#### **Task 1 – DOE Study to Investigate the Effect of Zirconium Addition, Pouring Temperature, and Settling Time on the Resultant Grain Size**

A Design of Experiments (DOE) approach was used to conduct a systematic study of the grain refinement behavior of magnesium by zirconium. The variables include the amount of zirconium addition, pouring temperature, and the settling time prior to casting. Samples were poured into a special mold designed to reproduce the conditions in permanent mold casting.

### *1.1 – DOE Matrix Based on the Magnesium-Zirconium Phase Diagram*

A DOE was conducted by varying three different parameters to study grain refinement efficacy: wt% total zirconium addition based on the magnesium-zirconium phase diagram (0.25, 0.5, and 1 wt %), pouring temperature (705 and 815°C), and settling time (0 and 30 min).

### *1.2 – Experimental Set-up*

An experimental setup was designed and developed to perform the grain refinement study of zirconium in magnesium. The mold was sectioned from 1018 steel pipe to form a ring mold. A gray iron block used as the chill. Samples were melted in a mild steel crucible using an electrical resistance furnace. A protective gas (0.5% SF<sub>6</sub> + CO<sub>2</sub>) mixture was used to prevent magnesium from burning. Zirconium in the form of magnesium-zirconium master alloy was stirred into the molten magnesium prior to casting. The mold, the chill and stirring rods were coated and preheated to 350°C.

### *1.3 – Analysis of Settling Behavior of Zirconium Particles*

The additions of zirconium to the magnesium melt result in the settling of zirconium particles in the bottom and the loss of its effectiveness as a grain refiner. The settling behavior of zirconium particles as a function of melt temperature and settling time is analyzed.

### *1.4 – Effect of Zirconium Addition, Pouring Temperature and Settling Time on the Final Microstructure*

The effect of the three process variables, zirconium addition, pouring temperature and settling time, on the resultant average grain size are analyzed and discussed.

## **Task 2 – TEM Study of Grain Refined Samples**

TEM (Tecnai F-20) was used to determine and establish the orientation relationship between the zirconium particles and the magnesium matrix. Bright Field (BF) micrographs and the associated selected area composite diffraction pattern (SADP) of the zirconium particle and the magnesium matrix provided insights on the potent nucleus and the grain refinement mechanism. High Resolution Transmission Electron Microscopy (HRTEM) technique was also used to observed the lattice mismatch and orientation relationship at the particle/matrix interface.

## **Task 3 – Analysis of Size, Shape, and Distribution of Zirconium Particles**

### *3.1 – Dissolution of Grain Refined Samples*

Sample of grain refined samples were dissolved into 1% diluted hydrochloric acid and kept for 72 hrs to digest the sample completely. The solution was centrifuged for 3 cycles. The final centrifuged sample was sonicated for 30 min and one drop of the solution was evenly distributed on a silicon wafer.

### *3.2 – Characterization of Dissolution Samples*

The dissolution samples were placed on a silicon wafer and dried and were characterized by SEM (JEOL 7000) to determine the particle morphology. The final centrifuged solution was also used to determine the particle size distribution using an Accusizer Model 770 instrument.

### *3.3 – Comparison of Grain Density with Faceted Particle Density*

Faceted zirconium particles evident from the SEM micrographs were counted to determine the number of faceted particles present in different grain refined samples. The fraction of the faceted particles were compared with each other. A calculation was performed to compare the grain

density with the faceted particle density to determine the nucleation efficiency of the faceted particles.

#### **Task 4 – Engineer a More Efficient Zirconium-based Grain Refiner for Magnesium Alloys**

##### *4.1 – ECAE Processing of Original Magnesium -15wt% Zirconium Master Alloy*

The goal of this task was to increase the grain refinement efficiency of the original master alloy by reducing the particle size. The original master alloy containing zirconium particles in the range of 0.5  $\mu\text{m}$  to 10  $\mu\text{m}$  was subjected to severe plastic deformation by Equal Channel Angular Extrusion (ECAE) at an elevated temperature to break up the large zirconium particles.

##### *4.2 – Characterization of the ECAE Processed and Original Master Alloys*

The ECAE processed and original master alloys were characterized using SEM and dissolution studies to get an understanding of the morphology and size distribution of the zirconium particles.

##### *4.3 – Grain Refinement Tests with ECAE Processed Master Alloy*

Grain refinement experiments were conducted with the ECAE processed and original master alloys to observe the grain refinement efficacy of the ECAE processed master alloy.

## 4. DESIGN OF EXPERIMENTS (DOE) STUDY

### 4.1 DOE Matrix Based on the Magnesium-Zirconium Phase Diagram

Pure magnesium (99.9% Mg) and magnesium-15 wt% zirconium grain refiner master alloy were used for the experiments. Three different parameters were varied to study grain refinement efficacy – wt% total zirconium addition (0.25, 0.5, and 1 wt %), pouring temperature (705 and 815°C), and settling time (0 and 30 min). The experimental DOE matrix is shown in Table 4.1. This is a full factorial experiment in one three-level factor and two two-level factors. A total of 12 grain refinement experiments were carried out. A pure magnesium hockey puck sample was also poured for comparison.

Table 4.1 Experimental DOE matrix

<b>Expt. No</b>	<b>wt% Zr</b>	<b>Temperature (°C)</b>	<b>Settling Time (min)</b>
1	0.25	705	0
2	0.25	705	30
3	0.25	815	0
4	0.25	815	30
5	0.50	705	0
6	0.50	705	30
7	0.50	815	0
8	0.50	815	30
9	1.0	705	0
10	1.0	705	30
11	1.0	815	0
12	1.0	815	30

The three levels of total zirconium addition were selected based on the magnesium-zirconium phase diagram as follows: less than the maximum solubility level of zirconium (0.25%), at the maximum solubility level of zirconium (0.5%), and equal to the current practice (1%). Fig. 4.1 shows the peritectic corner of the magnesium-zirconium phase diagram generated using Pandat software with the levels of zirconium addition used in this work [34]. The pouring temperatures were selected based on typical foundry practice for magnesium alloy castings. The settling time of 30 min was based on the time taken for zirconium particles 2  $\mu\text{m}$  diameter or greater to settle at least 20 mm, the height of the melt equivalent to one hockey puck in the mild steel crucible used for melting [25].

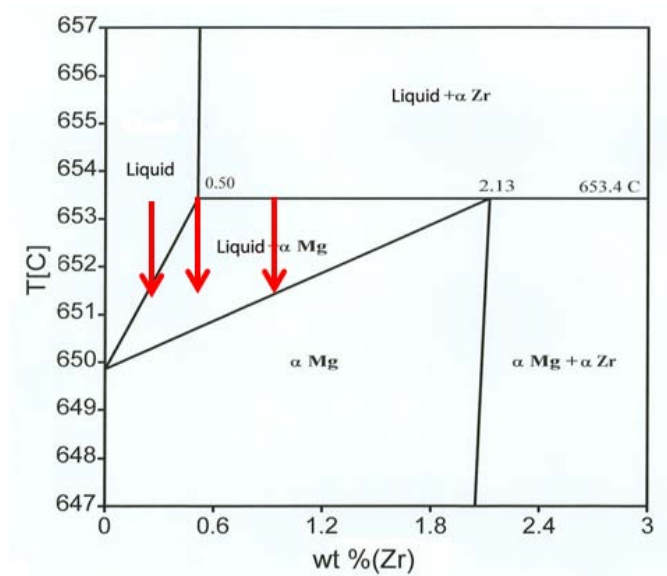


Fig. 4.1 Magnesium-Zirconium phase diagram showing experimental additions of 0.25, 0.5, and 1wt% zirconium.

#### 4.2 Experimental Set-up

Pure magnesium was melted in a mild steel crucible using an electrical resistance furnace (WENESCO; model MPM1B). The crucible was 45 mm in diameter and 160 mm tall, and the typical melt size was 250 g. The mold was sectioned from 1018 steel pipe to form a ring mold of

45 mm I.D., 63.5 mm O.D., and 12 mm height. A gray iron block, 100 x 100 x 25 mm, was used as the chill. The mold, the chill, and the stirring rod were coated with CONCOTE™MAG 669 (Hill and Griffith) prior to preheating to 350°C. Fig. 4.2 shows the casting setup used for this work. A protective gas mixture (0.5% SF<sub>6</sub> + CO<sub>2</sub>) was used to prevent magnesium from burning. Once the desired pouring temperature was reached, appropriate amounts of magnesium-15 wt% zirconium master alloy needed to obtain the various zirconium levels were added and allowed to dissolve for one minute. The melt was then stirred vigorously for 10 to 15 s with a coated mild steel rod and poured into the preheated (350°C) “hockey puck” mold to obtain the “0 min” sample. The melt was allowed to settle for 30 min and a second hockey puck mold was poured from the remaining melt to obtain the “30 min” sample.



Fig. 4.2 Hockey puck casting setup used for this work and the mild steel crucible used for the experiments.

### 4.3 Analysis of Settling Behavior of Zirconium Particles

SEM micrographs of the magnesium-15wt% zirconium master alloy used for this work show large zirconium particles and clusters at the grain boundaries as shown in Fig. 4.3. It is evident that the master alloy used for this work has large zirconium particles and particle clusters greater

than 5  $\mu\text{m}$  along the grain boundary. These zirconium particles do not take part in grain refinement and settle with time to the bottom of the crucible.

The settling of zirconium particles in the magnesium melt can be approximated [18] as

$$S \approx \frac{g(\rho_{\text{Zr}} - \rho_{\text{Mg}})d^2}{18\eta}t \quad (4.1)$$

where,  $S$  = settling distance = 20 mm for the melt height in the crucible during the experiment.

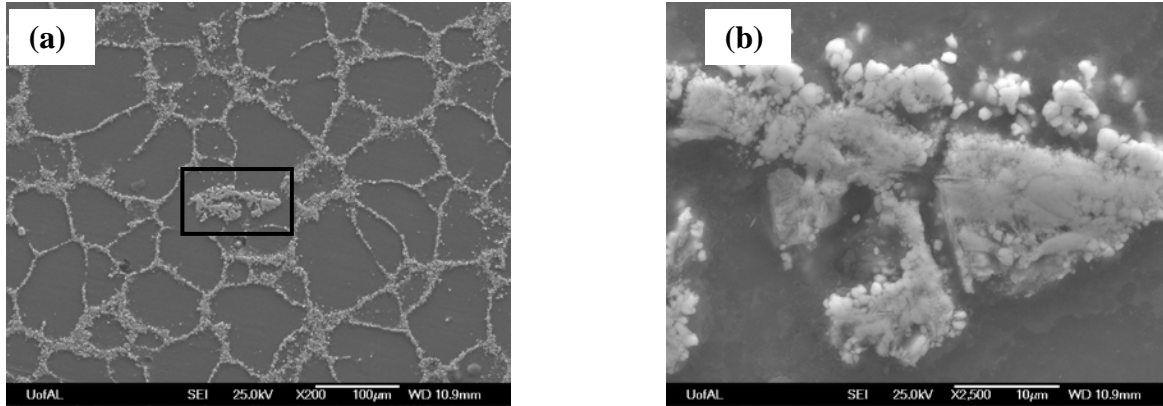


Fig. 4.3 (a) Scanning electron micrographs showing large zirconium particles and particle clusters along the grain boundary in magnesium-15wt% zirconium used for the work, (b) the enlarged view of the small marked region in (a).

The density of pure magnesium as a function of temperature is given as

$$\rho_{\text{Mg}}(T^{\circ}\text{C}) = 1.584 - 2.34 \times 10^{-4}(t - 650) \text{ g/cm}^3. \quad (4.2)$$

The density at  $705^{\circ}\text{C}$  was calculated as  $\rho_{\text{Mg}} = 1571.13 \text{ kg/m}^3$  and at  $815^{\circ}\text{C}$  as  $\rho_{\text{Mg}} = 1545.39 \text{ kg/m}^3$ .

The viscosity of pure magnesium in the temperature range of  $650\text{-}827^{\circ}\text{C}$  can be estimated as

$$\eta(T^{\circ}\text{C}) = 1.25 \times 10^{-3} - 2.54 \times 10^{-6}(T - 650) \text{ Nsm}^{-2}. \quad (4.3)$$

Viscosity at  $705^{\circ}\text{C}$  was calculated as  $\eta_{\text{Mg}} = 1.1103 \times 10^{-3} \text{ Nsm}^{-2}$  and at  $815^{\circ}\text{C}$   $\eta_{\text{Mg}} = 0.8309 \times 10^{-3} \text{ Nsm}^{-2}$ . The crucible used for the grain refinement is schematically shown in Fig. 4.4. The total melt size was 250 g which was equivalent to a melt height of 100 mm in the crucible after

melting. Based on the weight of a single hockey puck sample which is equal to 40 g, the equivalent height of the liquid melt was calculated as 20 mm.

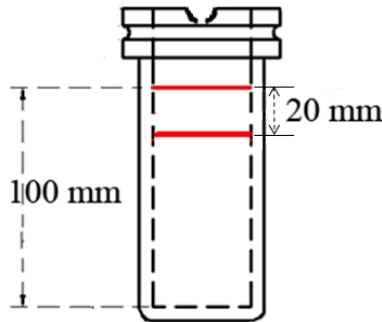


Fig. 4.4 A schematic diagram showing the mild steel crucible used for the grain refinement experiment. Note: The liquid melt height equivalent to one hockey puck was nearly equal to 20 mm.

Due to the settling of zirconium particles (fading) in the liquid magnesium melt, large zirconium particles will settle out and not take part in grain refinement. In this work, it is assumed that all the particles are uniformly distributed at the start of the melt, and that all zirconium particles greater than 2  $\mu\text{m}$  will travel more than 20 mm in 30 min, the melt height and equivalent to the weight of one hockey puck. Fig. 4.5(a) and (b) show the settling distance for various particles sizes for a settling time of 30 min for melt temperature of 705 and 815°C.

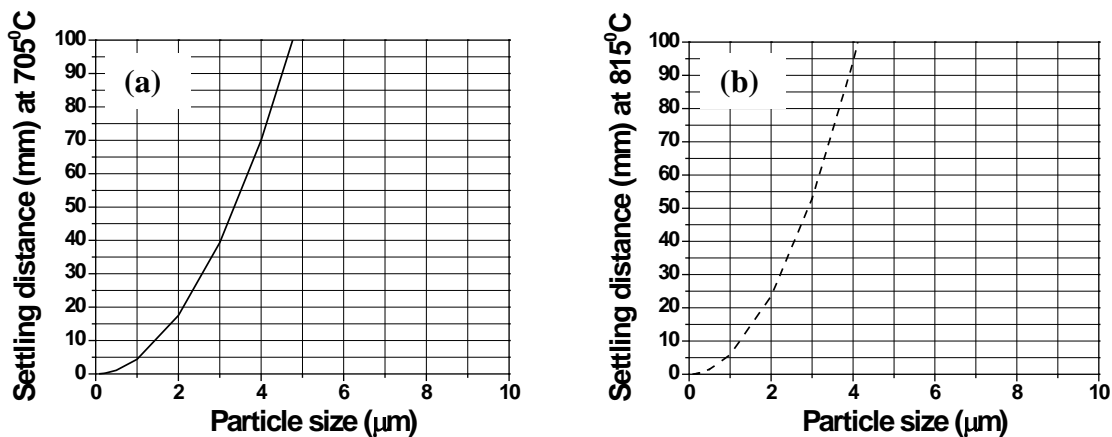


Fig.4.5 Settling distance for various particle sizes for a settling time of 30 min at (a) 705°C and (b) 815°C, predicted according to Eq. (4.1).

Fig. 4.6 relates particle size and settling time for a fixed settling distance of 20 mm. Fig. 4.6 shows that particles greater than 2  $\mu\text{m}$  particles will settle 20 mm in 30 min at a pouring temperature of 815°C.

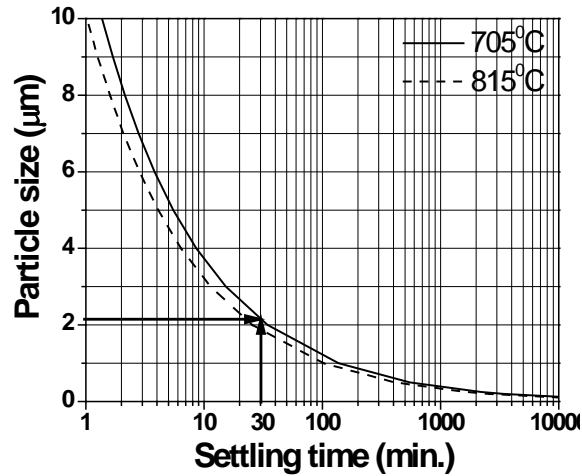


Fig. 4.6 Predicted settling behavior of different size of zirconium particles in pure magnesium melt as a function of pouring temperature.

#### 4.4 Results and Discussion

Metallographic specimens were sectioned from the center of the hockey puck using a Buehler Isomet<sup>®</sup> 1000 precision saw as shown in Fig. 4.7. Specimens were mounted in conductive epoxy using a hot compression mounting press (Buehler Simplimet<sup>®</sup> 1000). Mounted specimens were ground and polished using standard metallographic techniques<sup>†</sup> [<sup>†</sup> = see appendix]. The final polished samples were etched with an acetic picral solution (5 mL acetic acid, 6 g picric acid, 10 mL water and 100 mL ethanol) for 5 s. Optical micrographs were captured in polarized light with NIS-Elements image capturing/analysis software integrated with a NIKON EPIPHOT optical microscope. The grain size was measured 2 mm from the bottom of each hockey puck sample at 50x magnification using a standard grain size calculation method<sup>†</sup> [29, 30].

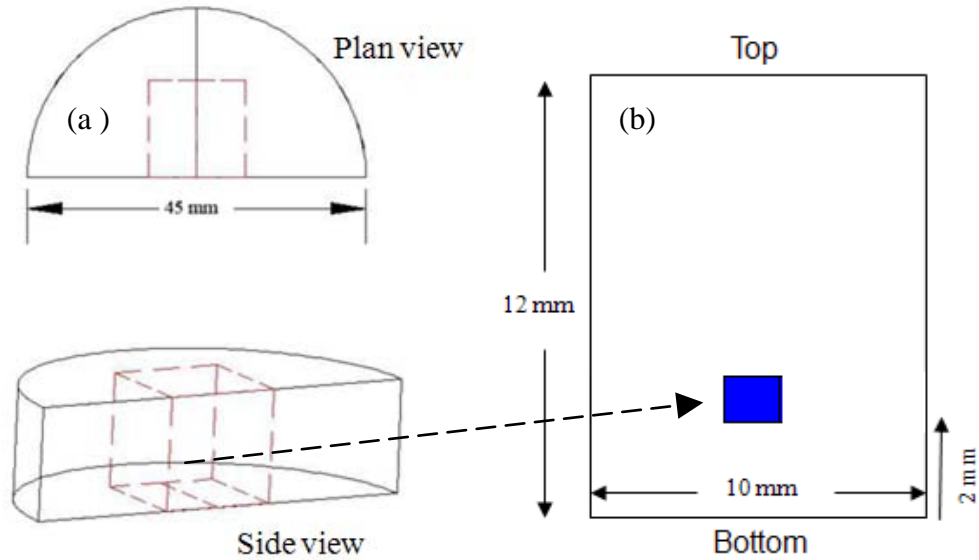


Fig. 4.7 (a) A schematic drawing of the hockey puck sample from the grain refinement experiments, and (b) location where grain size was measured, i.e. 2 mm from the bottom of the metallographic specimen.

Fig. 4.8 and 4.9 show optical micrographs in the unetched condition for magnesium-0.25 wt% zirconium samples poured at 815°C at settling times of 0 and 30 min. Large particles and clusters are evident at 0 min but are absent at 30 min, showing that large zirconium particles and particle clusters settle out with time.

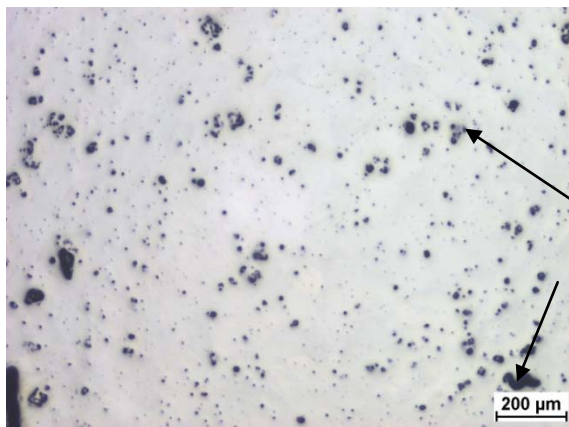


Fig. 4.8 Optical micrograph in the unetched condition for Mg-0.25 wt% Zr sample poured at 815°C at a settling time of 0 min.

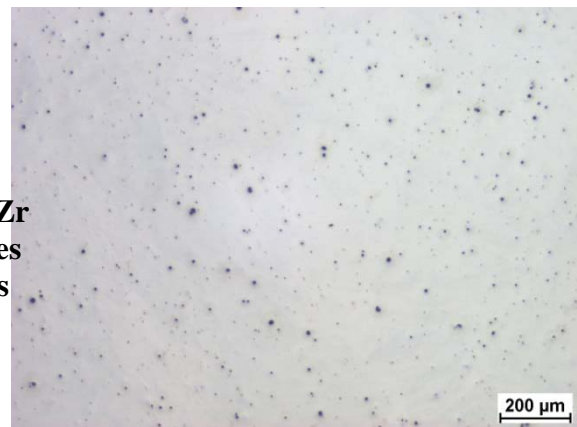


Fig. 4.9 Optical micrograph in the unetched condition for Mg-0.25 wt% Zr sample poured at 815°C at a settling time of 30 min.

#### 4.5 Effect of Zirconium Addition, Pouring Temperature, and Settling Time on the Final Microstructure

Fig. 4.10 shows an optical micrograph of a pure magnesium sample without any grain refiner addition. The microstructure in Fig. 4.10 shows large columnar grains, and deformation twins within the grains occur readily at normal temperature [5, 35] during grinding and polishing. Figs. 4.11 to 4.14 show optical micrographs of grain refined samples for total zirconium additions of 0.25, 0.5, and 1 wt% and pouring temperatures of 705 and 815°C. Figs. 4.11 through 4.14 show that for samples poured at 815°C, the measured grain size decreases with increasing zirconium level but is consistently larger at a settling time of 30 min. The results are similar for a pouring temperature of 705°C, except at the 0.25 wt% zirconium level, in which no grain refinement was observed at 0 min. Also, the measured grain size is somewhat larger at 705°C compared to 815°C for similar zirconium levels and settling times. Importantly, a comparison of Fig. 4.10, Fig. 4.13(a), and 4.14(a) confirms that the peritectic reaction is not needed for grain refinement.

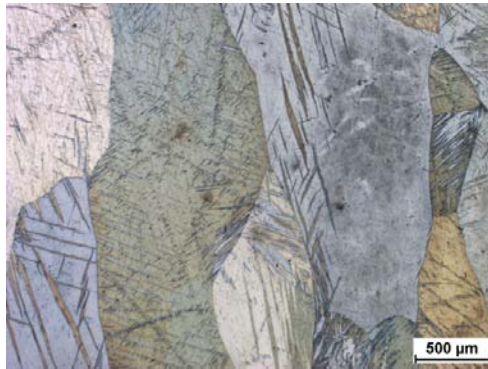
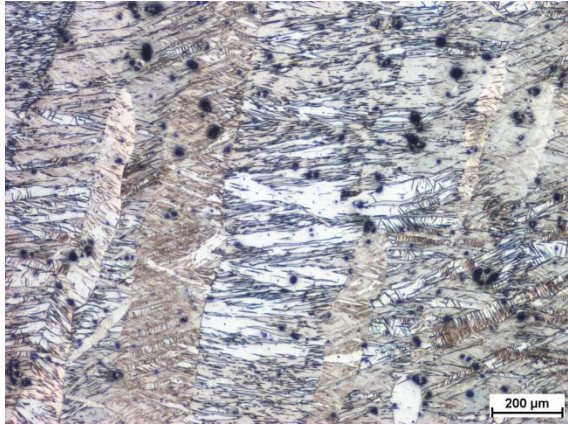


Fig. 4.10 Optical micrograph of pure magnesium hockey puck sample without any grain refiner addition (magnification 25x).

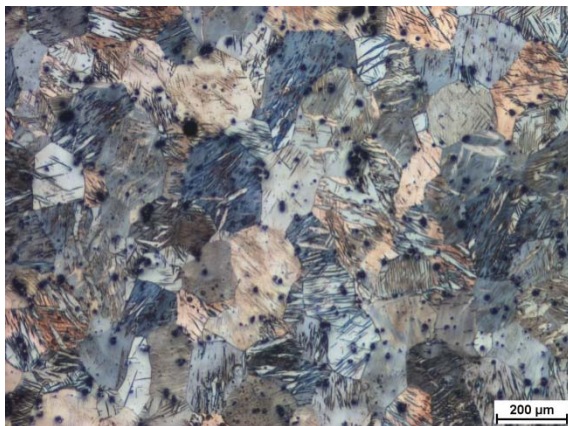
Figs. 4.15, 4.16, and 4.17 show the variation of the measured grain size with zirconium addition, pouring temperature, and settling time. Grain size decreases with increasing zirconium additions for both pouring temperatures and settling times. A smaller grain size is generally obtained at the higher pouring temperature.



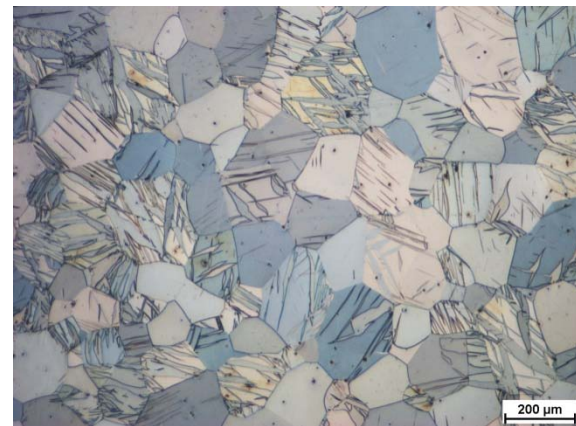
(a) 490  $\mu\text{m}$



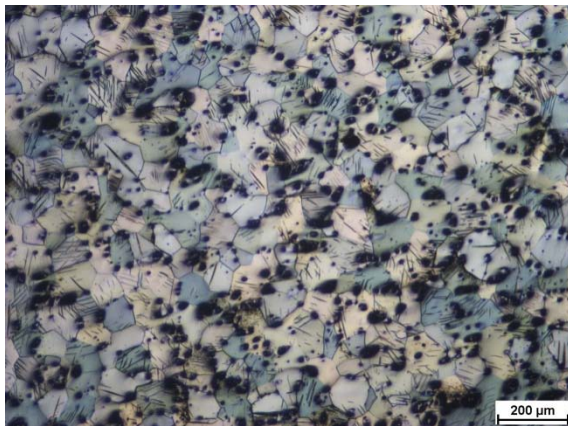
(a) 252  $\mu\text{m}$



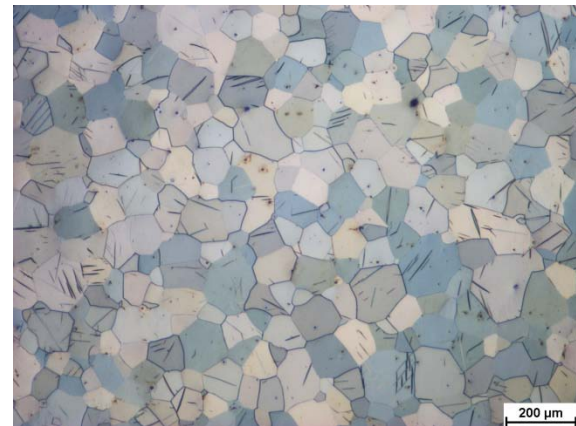
(b) 118  $\mu\text{m}$



(b) 138  $\mu\text{m}$



(c) 65  $\mu\text{m}$



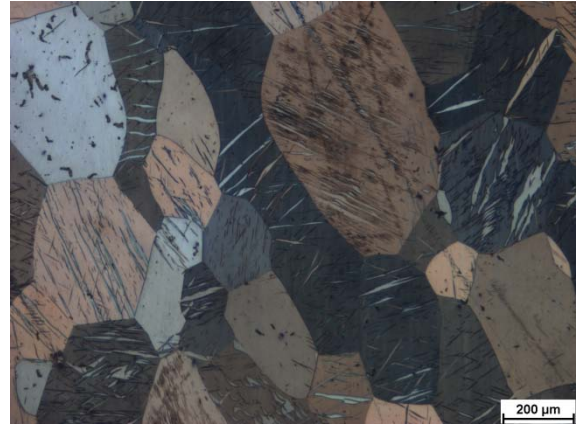
(c) 78  $\mu\text{m}$

Fig. 4.11 Optical micrographs of samples poured at 705°C and a settling time of 0 min for a) 0.25 wt% zirconium, b) 0.5 wt% zirconium, and c) 1 wt% zirconium. The measured grain size is indicated below each micrograph (magnifications 50x).

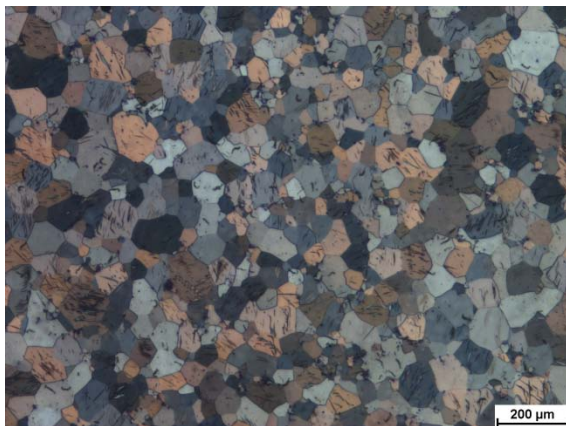
Fig. 4.12 Optical micrographs of samples poured at 705°C and a settling time of 30 min for a) 0.25 wt% zirconium, b) 0.5 wt% zirconium, and c) 1 wt% zirconium. The measured grain size is indicated below each micrograph (magnifications 50x).



(a) 109 μm



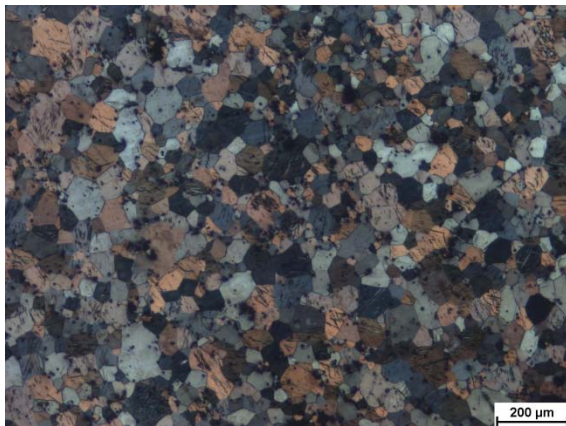
(a) 230 μm



(b) 59 μm



(b) 82 μm



(c) 51 μm



(c) 60 μm

Fig. 4.13 Optical micrographs of samples poured at 815°C and a settling time of 0 min for a) 0.25 wt% zirconium, b) 0.5 wt% zirconium, and c) 1 wt% zirconium. The measured average grain size is indicated below each micrograph (magnifications 50x).

Fig. 4.14 Optical micrographs of samples poured at 815°C and a settling time of 30 min for, a) 0.25 wt% zirconium, b) 0.5 wt% zirconium, and c) 1 wt% zirconium. The measured average grain size is indicated below each micrograph (magnifications 50x).

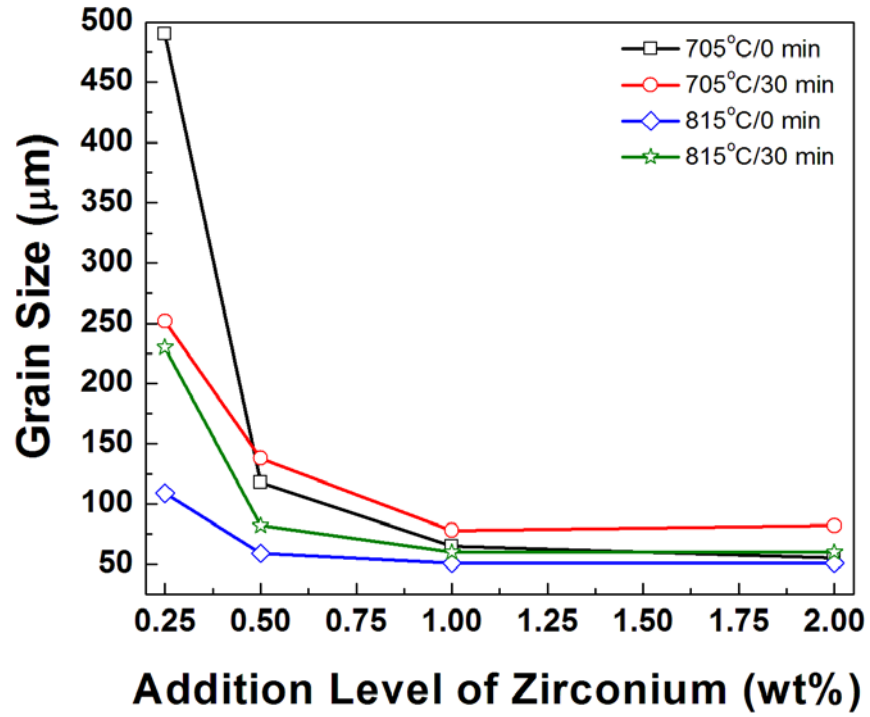


Fig. 4.15 Measured grain size vs. zirconium addition.

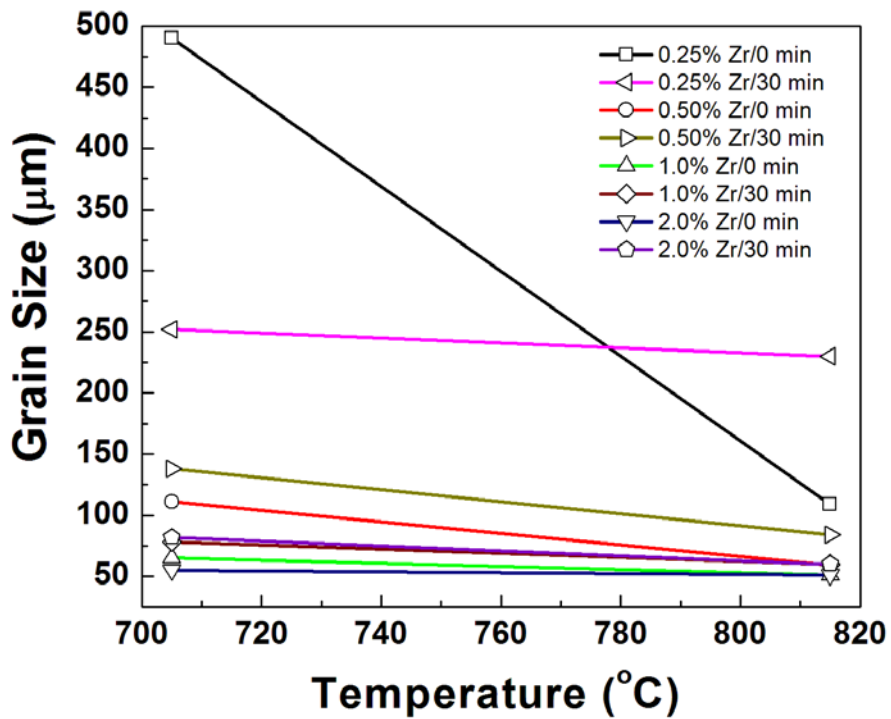


Fig. 4.16 Measured grain size vs. pouring temperature.

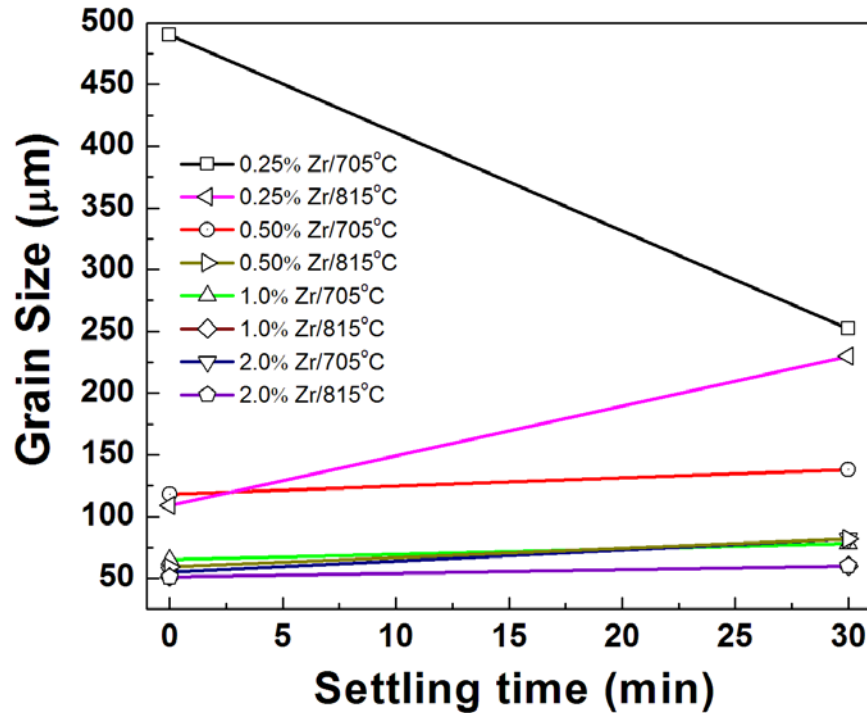


Fig. 4.17 Measured grain size vs. settling time.

A settling time of 30 min generally results in a larger grain size, except for an addition of 0.25 wt% zirconium at 705°C, when no grain refinement was observed at 0 min.

This work attempted to use 2 µm as a target zirconium particle size by the use of a settling time of 30 min that allowed particles greater than 2 µm to settle out. However, the fact that grain size was consistently larger at the 30 min settling time suggests that particles larger than 2 µm may contribute to grain refinement. The results show that zirconium additions less than that needed for the peritectic reaction can produce grain refinement. However, Figure 4.15 clearly shows that for the zirconium-15 wt% zirconium master alloy used in this work, an addition of 1 wt% zirconium produces the smallest grain size. Addition of 2 wt% zirconium did not result in a decrease of the grain size. It is likely that the 1 wt% addition provides the requisite number of suitable nuclei for maximum grain refinement. Consequently, any attempt to engineer a more efficient grain refiner must target both particle size and number.

## 4.6 Conclusion

A systematic DOE study of the grain refinement of magnesium by zirconium showed that the peritectic reaction is not needed for grain refinement. The measured grain size was consistently larger at the 30 min settling time, suggesting that large particles larger than 2  $\mu\text{m}$  may contribute to grain refinement. For the grain refiner master alloy used, 1 wt% zirconium addition, equal to that used in current practice, produced the best grain refinement. However, based on the fact that a significant amount of zirconium is wasted, it appears likely that with a properly engineered magnesium-zirconium master alloy, zirconium additions considerably less than currently used could result in effective grain refinement.

## 5. TRANSMISSION ELECTRON MICROSCOPY (TEM) STUDY OF PARTICLE SIZE, AND ORIENTATION

### 5.1 Introduction

In the literature, there is no strong microscopic evidence of nucleant particles and the selection rule for the crystallization of grains. Greer [18, 36] showed in a TEM investigation on a metallic glass sample grain refined with Al-5Ti-1B grain refiner, that hexagonal platelets of  $\text{TiB}_2$  particles with a  $\{0001\}$  basal plane act as suitable nucleation sites for aluminum growth. However, the  $\{0001\}$  faces of the  $\text{TiB}_2$  were coated with a thin layer of  $\text{Al}_3\text{Ti}$ , which is the actual nucleation substrate for  $\alpha$ -aluminum crystal. Schumacher [37] showed that a well defined orientation relationship exists between all three phases. The orientation relationship was given as  $\{111\}_{\text{Al}} \parallel \{0001\}_{\text{TiB}_2} \parallel \{112\}_{\text{Al}_3\text{Ti}}$  and  $\langle 110 \rangle_{\text{Al}} \parallel \langle 11-20 \rangle_{\text{TiB}_2} \parallel \langle 110 \rangle_{\text{Al}_3\text{Ti}}$ . Greer pointed out that the TEM investigation does not shed any light on why only 1% of particles succeed in nucleating grains whereas all the particles observed with the TEM appear to be acceptable nucleants.

Naglić *et al.* [38] investigated the orientation relationship (OR) between TiC particles and the surrounding  $\alpha$ -aluminum matrix. In their experimental study performed on commercial purity aluminum by the addition of  $\text{AlTiC}_{0.15}$  grain refiner master alloy, they concluded that nucleation takes place on the  $\{111\}$  planes of TiC such that identical  $\{111\}$  planes in both crystals are in parallel orientation. Cisse *et al.* [8] studied the nucleation of aluminum on TiC particles and observed that epitaxial growth of aluminum occurs on the TiC particles where the orientation relationship is  $(001)_{\text{Al}} \parallel (001)_{\text{TiC}}$  and  $[001]_{\text{Al}} \parallel [001]_{\text{TiC}}$ .

Mayes *et al.* [39] found  $\text{TiAl}_3$  particles in a commercial Al-Ti-C master alloy used for grain refinement of aluminum had different morphologies ranging from well faceted to rough and irregular, whereas TiC individual particles were in the shape of a octahedron with a well defined {111} facet plane. They also concluded that undissolved TiC particles from the master alloy were the most likely nucleation substrate for aluminum grains.

In the magnesium-zirconium system there is no detailed microscopic evidence of the size and the shape of the zirconium particles which act as nucleation sites for crystallizing magnesium grain. Qian *et al.* [40] reported that undissolved zirconium particles as well as zirconium that precipitates out from the melt during cooling can act as nucleants for magnesium grains. The zirconium particles they observed under SEM in the back scattered electron mode were of different sizes and irregular in shape but they failed to prove whether the particles acted as nucleation sites or not as no orientation relationships were determined.

## **5.2 TEM Study of Grain Refined Samples**

In this study TEM analysis was performed to identify zirconium particles in grain refined samples that are likely nucleation sites. TEM bright field (BF) microscopy and selected area composite diffraction patterns (SADP) were used to analyze the particle-matrix orientation relationship. For particles which were not electron transparent, high resolution TEM (HRTEM) was used to determine orientation relationships at the particle-matrix interface. The TEM bright field micrographs and diffraction patterns were taken using a FEI Tecnai F-20 TEM operating at 200 keV.

### 5.3 Results and Discussion

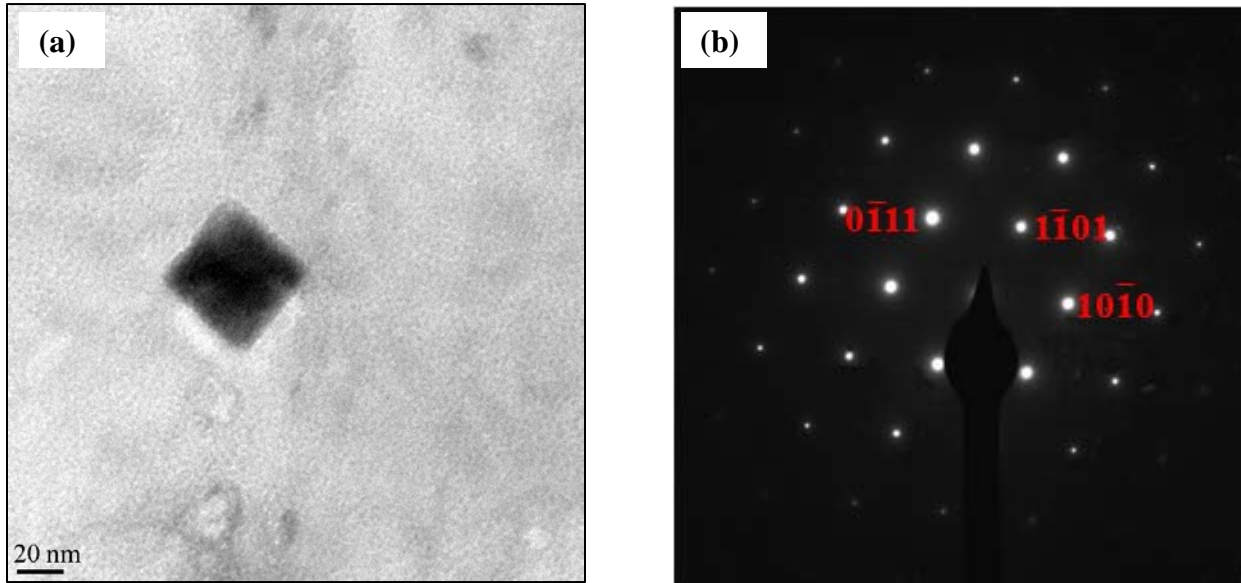


Fig. 5.1 (a) Bright field (BF) micrograph of a zirconium precipitate (50 nm) embedded within magnesium matrix, (b) composite selected area diffraction pattern (SADP) of magnesium matrix and the zirconium particle, the particle shows a parallel axis orientation relationship with matrix. Electron beam is parallel with  $[1\bar{2}\bar{1}3]$  direction.

Fig. 5.1(a) shows a bright field TEM image of a faceted zirconium particle (50 nm) embedded within the magnesium matrix from the magnesium-1.0 wt% zirconium grain refined sample (pouring temperature = 815°C, settling time = 30 min). The selected area composite diffraction pattern (SADP) of the particle and the matrix illustrated in Fig. 5.1(b) reveals a parallel axis orientation relationship. The diffraction spot from the matrix and the particle were superimposed on each other. The orientation relationship between the precipitate and the matrix was determined as  $(10\bar{1}1)_{\text{Mg}} \parallel (10\bar{1}1)_{\text{Zr}}$  and  $[\bar{1}\bar{2}\bar{1}3]_{\text{Mg}} \parallel [\bar{1}\bar{2}\bar{1}3]_{\text{Zr}}$ . The planar discrepancy between the low-index planes was very small. The similarity in the crystal structure and similar lattice spacings between magnesium and zirconium supports the fact that zirconium particles which are likely nucleation sites will show a parallel axis orientation with the matrix.

Various particles from a grain refined sample (magnesium-0.5% zirconium, 815°C, 30 min) were observed under TEM. Bright field micrographs of particles with selected area diffraction patterns were used to determine whether the particle was a nucleation site or not. Fig. 5.2(a) shows a small faceted zirconium particle 0.23  $\mu\text{m}$  in size at the center of a magnesium grain. The selected area composite diffraction pattern of the particle and the matrix illustrated in Fig. 5.2(b) shows that a parallel axis orientation relation exists between the particle and the matrix. The diffraction spots were indexed based on the  $[2\bar{1}\bar{1}0]$  direction of the hcp crystal. All the diffraction spots from the matrix and the particle were exactly superimposed on each other. The orientation relationship between the particle and the matrix was established as  $(0001)_{\text{Mg}} \parallel (0001)_{\text{Zr}}$  and  $[2\bar{1}\bar{1}0]_{\text{Mg}} \parallel [2\bar{1}\bar{1}0]_{\text{Zr}}$ . The fact that the particle shows a parallel axis orientation with the matrix suggests that the particle is a likely nucleation site for the magnesium grain.

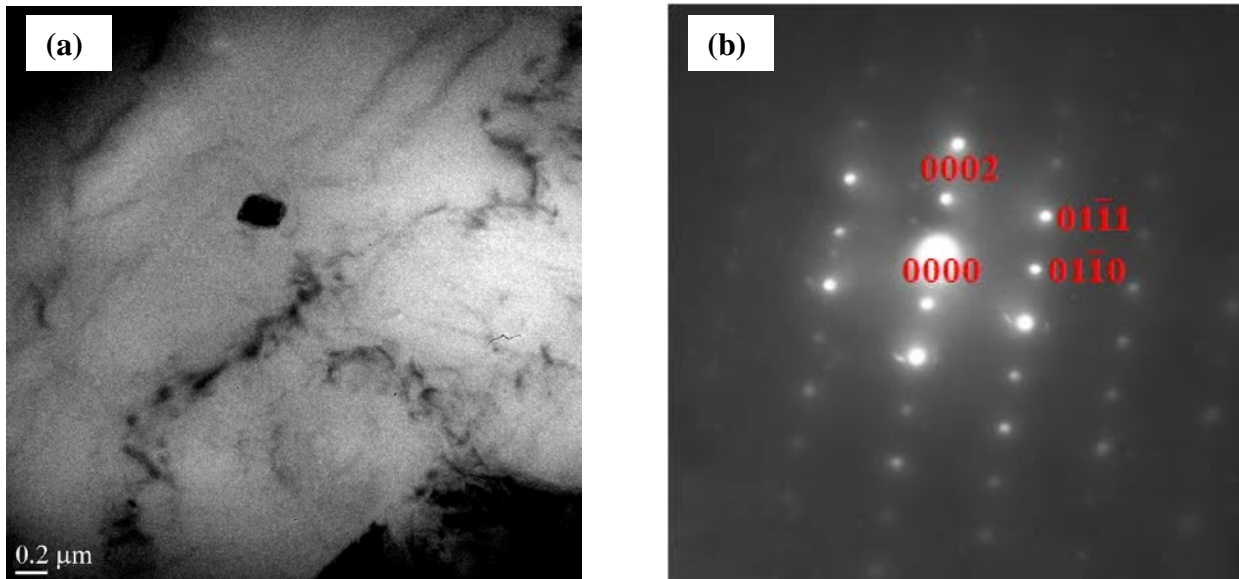


Fig. 5.2 (a) TEM bright field micrograph showing a faceted zirconium particle (equivalent diameter of the particle is 0.23  $\mu\text{m}$ ) embedded in the magnesium matrix, and (b) composite selected area diffraction pattern (SADP) taken with electron beam parallel to  $[2\bar{1}\bar{1}0]$  direction from the matrix and the particle.

Fig. 5.3(a) shows a medium sized zirconium particle of 0.5  $\mu\text{m}$  found at the thin section of the TEM foil. The selected area diffraction pattern from the matrix and the particle depicted in Figs. 5.3(b) and (c) show a parallel orientation relationship. The electron beam was tilted toward the  $[01\bar{1}0]$  direction of the foil plane to determine the diffraction pattern. The presence of a 0001 forbidden diffraction spot was due to the zirconium particle. The particle shows an exact parallel orientation relationship  $[01\bar{1}0]_{\text{Mg}} \parallel [01\bar{1}0]_{\text{Zr}}$  with the matrix suggesting that the particle was a likely nucleation site for the crystallized magnesium grain.

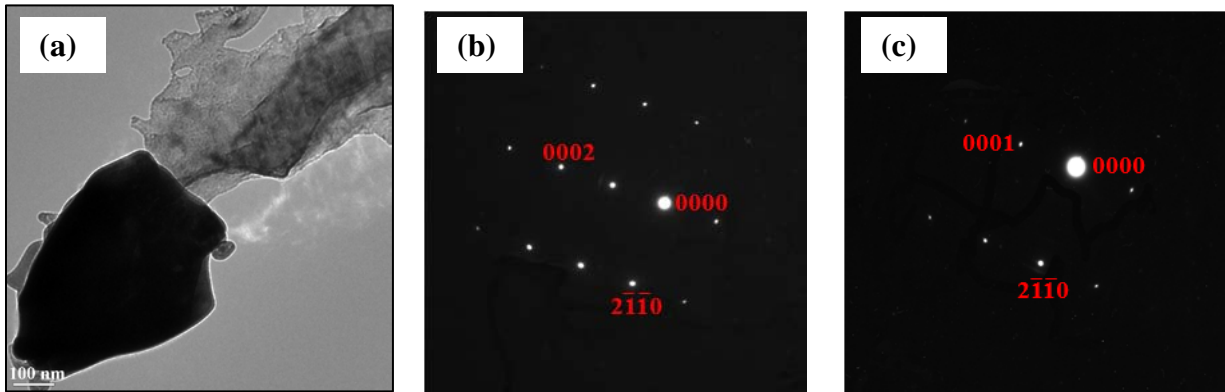


Fig. 5.3 (a) Bright field (BF) micrograph of a faceted zirconium particle (equivalent size of 0.5  $\mu\text{m}$ ) found within magnesium matrix, (b) selected area composite diffraction pattern (SADP) of particle and matrix, and (c) of the particle. The particle shows a parallel axis orientation relationship with the matrix.

Fig. 5.4(a) illustrates a large faceted zirconium particle (length: 1.6  $\mu\text{m}$  and the width: 1  $\mu\text{m}$ ) embedded in the magnesium matrix at the center of a single grain from the magnesium-0.5 % zirconium 815°C-30 min grain refined sample. The bright field micrograph suggests that the particle was faceted in nature. The composite selected area diffraction pattern shown in Fig. 5.4(b) for the particle and matrix reveals that a parallel axis orientation relationship exists between the particle and matrix. The diffraction spots were indexed from the standard  $[2\bar{1}\bar{1}0]$  diffraction pattern of a hcp magnesium crystal.

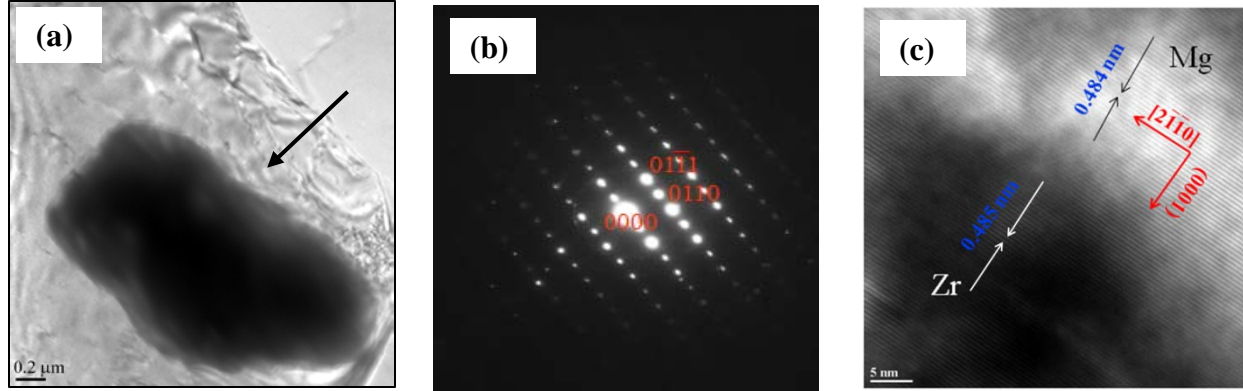


Fig. 5.4 (a) Bright field (BF) micrograph of a zirconium particle (length: 1.6  $\mu\text{m}$  and the width: 1  $\mu\text{m}$ ) embedded within magnesium matrix, (b) composite selected area diffraction pattern (SADP) of magnesium matrix and the particle, and (c) HRTEM lattice fringe image at the particle/matrix interface showing continuous lattice fringes. The interplanar spacing for the (0001) plane was measured 0.484 nm and the 0.485 nm in the matrix and particle respectively along the  $[2\bar{1}\bar{1}0]$  direction, No dislocation or atomic misfit was observed at the particle/matrix interface suggesting the particle could be a potent nucleation site for the magnesium matrix.

High resolution TEM (HRTEM) was performed at the particle/matrix interface. The lattice fringes clearly suggest that the particle was completely coherent with the matrix as there was no atomic misfit or dislocation observed at the interface. The result provides an insight into the fact that the magnesium grain grew epitaxially on a suitable plane of the zirconium crystal. The interplanar spacing was measured along the (0001) plane of magnesium and the  $[2\bar{1}\bar{1}0]$  direction of the zirconium particle as 0.484 and 0.485 nm respectively. Treilleux [41] determined the orientation relationship between a lithium precipitate and a magnesium oxide single crystal from the lattice fringes of the respective crystals. He showed that if the fringe spacing is known for the matrix ( $d_0$ ) and the precipitate ( $d_1$ ) then the interplanar lattice disregistry or misfit is given by:

$$\delta = \frac{d_0 - d_1}{\frac{d_0 + d_1}{2}} \cong \frac{d_0 - d_1}{d_0} \quad (5.1)$$

For the particle shown in Fig. 5.4 the lattice registry between the particle and the matrix was calculated as 0.2%. The orientation relationship between the zirconium particle and the matrix was determined as  $(0001)_{\text{Mg}} \parallel (0001)_{\text{Zr}}$  and  $[2\bar{1}\bar{1}0]_{\text{Mg}} \parallel [2\bar{1}\bar{1}0]_{\text{Zr}}$ .

Figs. 5.2 to 5.4 show that different sizes of particles that are likely nucleation sites were observed from the same grain refined sample (magnesium-0.5% zirconium, pouring temperature = 815°C, and settling time = 30 min), suggesting that a range of zirconium particles (0.23  $\mu\text{m}$  to 1.6  $\mu\text{m}$ ) were likely nucleation sites. The above result can be explained by Greer's free growth model which suggests that different sizes of substrates will become active when the required undercooling is reached.

Fig. 5.5(a) shows a faceted zirconium particle obtained from a magnesium-0.5 wt% zirconium grain refined sample (pouring temperature = 815°C, and settling time = 0 min). The selected area diffraction patterns from the matrix and the particle depicted separately in Figs. 5.5(b) and (c) reveal diffraction spots that can be superimposed on each other.

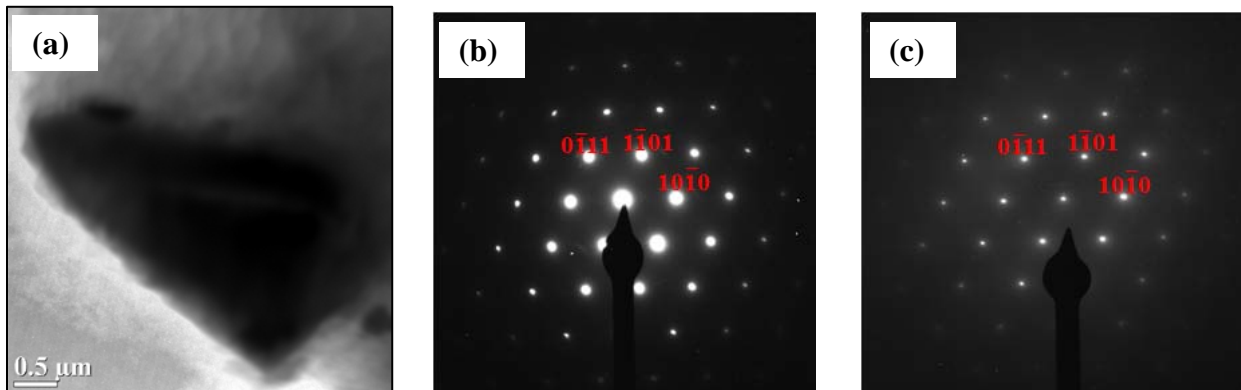


Fig. 5.5 (a) Bright field (BF) micrograph of a faceted zirconium particle 4  $\mu\text{m}$  in size embedded within the magnesium matrix, (b) selected area diffraction pattern (SADP) from the matrix, and (c) zirconium particle. The diffraction spots from each pattern were superimposed on each other. A parallel axis orientation relationship exists between the particle and the matrix. The electron beam is parallel with  $[\bar{1}\bar{2}\bar{1}3]$  direction. The intensity of the diffraction spots from the particle was weak due to thickness of the particles.

The particle and matrix showed a near parallel axis orientation relationship, and a  $[\bar{1}2\bar{1}3]_{Mg} \parallel [\bar{1}2\bar{1}3]_{Zr}$  type orientation relationship was established from the diffraction pattern. The intensity of the diffraction spots from the zirconium particle was weak due to the thickness of the particle.

It is quite apparent from all the above TEM study that only faceted particles show a parallel axis orientation relationship with the matrix and are likely nucleation sites. However, not all particles act as nucleation centers. Several particles were found that show a large misorientation with the matrix. Fig. 5.6(a) shows a zirconium particle (length: 1.4  $\mu\text{m}$  and width: 0.6  $\mu\text{m}$ ) embedded in the magnesium matrix. The selected area diffraction patterns from the matrix and the particle in Figs. 5.6(b) and (c) show that particle was misoriented  $\sim 28^\circ$  from the matrix. The selected area diffraction pattern from the matrix reveals that the foil plane was normal to the  $[2\bar{1}\bar{1}0]$  direction. However the electron beam was rotated a further  $28^\circ$  in the  $\beta$  direction (using the FEI double tilt holder) to get the particle electron diffraction pattern. The particle was indexed with a  $[2\bar{1}\bar{1}0]$  direction. The planar lattice disregistry was calculated using Bramfitt's formula [42]:

$$\delta_{(0001)_{Mg}}^{(0001)_{Zr}} = \frac{d_{Zr} \cos \theta - d_{Mg}}{d_{Mg}} \quad (5.2)$$

The lattice disregistry ( $\delta$ ) was calculated as 11.1% between the matrix and the zirconium particle. Since the lattice disregistry was very high, it is likely that the zirconium particle was not a nucleation site for the magnesium grain. The orientation relationship was determined as  $(0001)_{Mg} \wedge (0001)_{Zr}$  by  $28^\circ$  and  $[2\bar{1}\bar{1}0]_{Mg} \parallel [2\bar{1}\bar{1}0]_{Zr}$ .

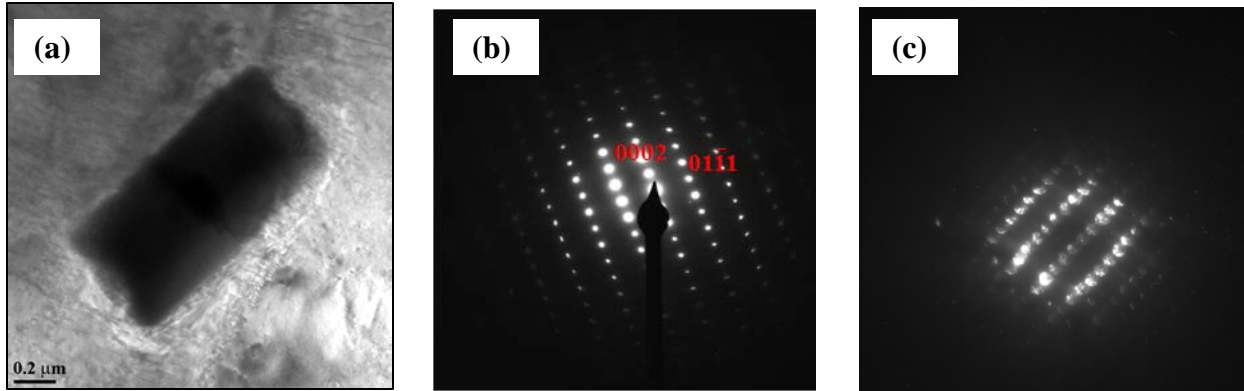


Fig. 5.6 (a) Bright field (BF) micrograph of a zirconium particle (length: 1.4  $\mu\text{m}$  and the width: 0.6  $\mu\text{m}$ ) embedded within magnesium matrix, (b) corresponding selected area diffraction pattern (SADP) of magnesium matrix, and (c) of the zirconium particle. The particle shows a large angle ( $\sim 28^\circ$ ) of misorientation with the matrix.

Several other particles were found at the grain boundaries and did not show any orientation relationship with the matrix (Fig. 5.7). This suggests that not all particles are selected as nucleation sites and cause grain refinement.

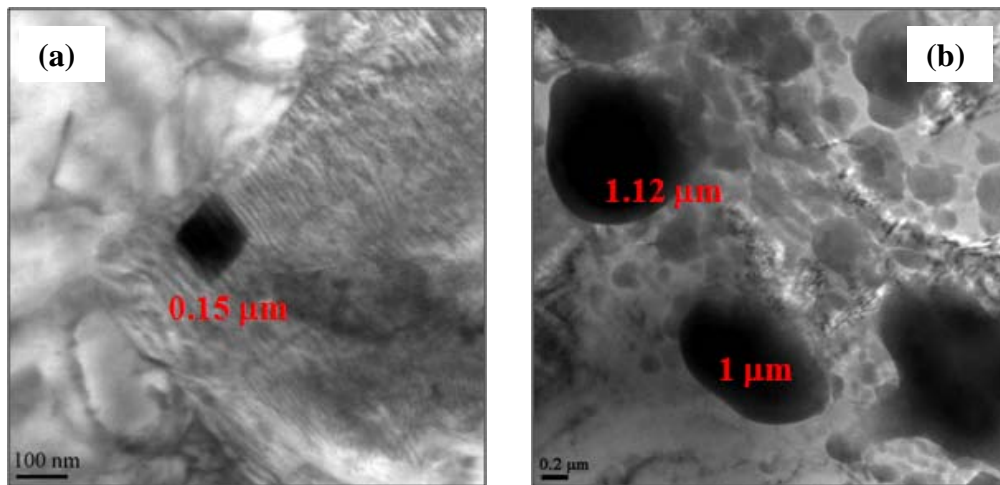


Fig. 5.7 (a) Bright field (BF) micrograph of a 0.15  $\mu\text{m}$  zirconium particle, (b) two different particles of 1  $\mu\text{m}$  and 1.2  $\mu\text{m}$  found at the grain boundaries did not show any orientation relationship with the matrix suggesting that not all the particles selected for grain refinement. The particles were observed in the magnesium-1% zirconium (pouring temperature = 815 $^\circ\text{C}$ , and settling time = 30 min) grain refined sample.

High resolution transmission electron microscopy (HRTEM) was performed to identify a likely nucleation site. Fig. 5.8(a) illustrates a faceted zirconium particle 0.5  $\mu\text{m}$  in size found in the magnesium-0.5% zirconium grain refined sample (pouring temperature = 815°C, and settling time = 30 min) embedded within the matrix. The composite selected area diffraction pattern shown in Fig. 5.8(b) clearly suggests that the particle had a nearly parallel axis orientation relationship with the matrix. However it was evident from the diffraction pattern that the  $(11\bar{2}2)_{\text{Zr}}$  plane of the zirconium particle was slightly ( $1^\circ$ ) misoriented from the  $(11\bar{2}2)_{\text{Mg}}$  matrix. All other diffraction spots from the matrix and the particle were exactly superimposed on each other. The electron beam was parallel to the  $[\bar{1}2\bar{1}3]$  direction of the hcp crystal. The orientation relationship between the zirconium particle and the matrix was determined as follow  $(11\bar{2}2)_{\text{Mg}} \wedge (11\bar{2}2)_{\text{Zr}}$  by  $1^\circ$  and  $[\bar{1}2\bar{1}3]_{\text{Mg}} \parallel [\bar{1}2\bar{1}3]_{\text{Zr}}$ . The high resolution TEM (HRTEM) image of the particle/matrix

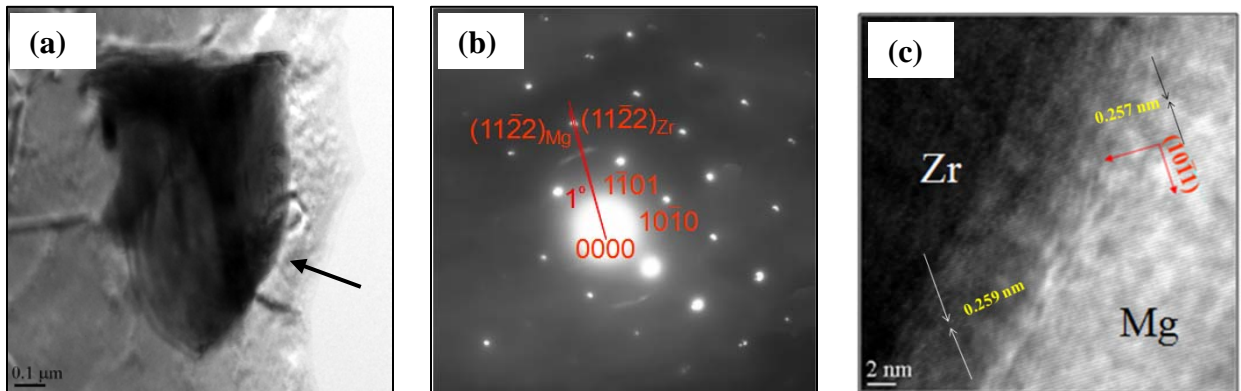


Fig. 5.8 (a) Bright field (BF) micrograph of a zirconium particle 0.5  $\mu\text{m}$  size embedded within magnesium matrix, (b) composite selected area diffraction pattern (SADP) of the matrix and the particle show low angle of misorientation between the  $(11\bar{2}2)$  plane of zirconium and magnesium, Electron beam parallel with  $[\bar{1}2\bar{1}3]$  direction (c) HRTEM image showing lattice fringes at the particle-matrix interface. The interplanar spacing was measured 0.257 nm in the matrix and 0.259 nm in the particle for the  $(10\bar{1}1)$  plane.

interface is shown in Fig. 5.8(c). Continuous lattice fringes from the matrix and the particle clearly suggest that particle was completely coherent with the matrix as there was no evidence of

atomic misfit or dislocation at the interface. The result suggests that the magnesium grain was grown epitaxially on a suitable plane of the zirconium crystal. The interplanar spacing was measured as 0.257 and 0.259 nm in the matrix and particle, respectively, suggesting that the lattice mismatch between the planes of the matrix and particle was very small. The lattice disregistry ( $\delta$ ) between the particle and the matrix was calculated as 0.13% for the above case. Though the HRTEM shows continuous lattice fringes, a low lattice mismatch still exists at the interface.

Similar analysis from the same grain refined sample shows another particle of 0.6  $\mu\text{m}$  in size depicted in Fig. 5.9(a). High resolution TEM (HRTEM) analysis was performed at the particle-matrix interface near the electron transparent area of the TEM foil. The interface shows clear atomic misfit where the (0001) planes were tilted from each other by a large angle dislocation boundary. The interplanar spacing was measured as 0.320 and 0.322 nm in the matrix

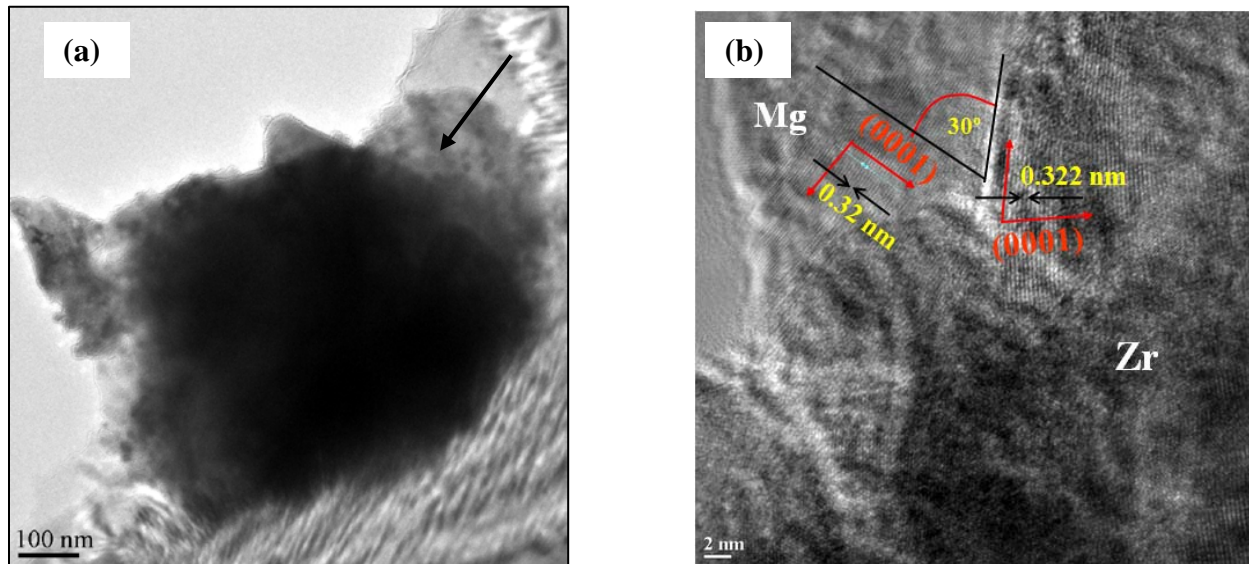


Fig. 5.9 (a) Bright field (BF) micrograph of a zirconium particle of 0.6  $\mu\text{m}$  in size found within magnesium matrix, (b) high resolution TEM image showing lattice fringes at the particle/matrix interface. The interplanar spacing between the fringes was measured 0.320 nm in the matrix and 0.322 nm in the particle for the (0001) plane. Clear atomic misfit was observed at the particle/matrix interface suggesting that the particle was not a likely nucleation site.

and particle, respectively. It is observed that the lattice fringes from the matrix and the particle along the (0001) plane shown Fig. 5.9(b) were completely incoherent. The lattice disregistry ( $\delta$ ) between the particle and the matrix was calculated as 12.9% for the above case. The orientation relationship between the particle and matrix was established as  $(0001)_{\text{Mg}} \wedge (0001)_{\text{Zr}}$  by  $30^\circ$ . This particle likely did not act as a nucleation site for the magnesium grain.

Table 5.1 shows the detail orientation relationships that exist between the particle and the matrix. It is evident from the table that particles which are likely nucleation sites are faceted, show a small planar disregistry ( $\sim 0.1\text{-}0.2\%$ ), and exhibit a parallel axis orientation relationship with the matrix.

TABLE 5.1 Calculation of planar lattice disregistry and orientation relationship between zirconium nucleus and magnesium matrix for different grain refined samples

Particle size (equivalent diameter)	Orientation Relationship	Misorientation	Lattice Disregistry	Nucleation site
50 nm (faceted)	$(10\bar{1}1)_{Mg} \parallel (10\bar{1}1)_{Zr}$ and $[\bar{1}2\bar{1}3]_{Mg} \parallel [\bar{1}2\bar{1}3]_{Zr}$	parallel axis orientation	small	yes
0.23 $\mu\text{m}$ (faceted)	$(0001)_{Mg} \parallel (0001)_{Zr}$ and $[2\bar{1}\bar{1}0]_{Mg} \parallel [2\bar{1}\bar{1}0]_{Zr}$	parallel axis orientation	very small	yes
0.5 $\mu\text{m}$ (faceted)	$[01\bar{1}0]_{Mg} \parallel [01\bar{1}0]_{Zr}$	parallel axis orientation	very small	yes
length: 1.6 $\mu\text{m}$ and width: 1 $\mu\text{m}$	$(0001)_{Mg} \parallel (0001)_{Zr}$ and $[2\bar{1}\bar{1}0]_{Mg} \parallel [2\bar{1}\bar{1}0]_{Zr}$	parallel axis orientation	0.2%	yes
4 $\mu\text{m}$ (faceted)	$[\bar{1}2\bar{1}3]_{Mg} \parallel [\bar{1}2\bar{1}3]_{Zr}$	parallel axis orientation	very small	yes
length: 1.4 $\mu\text{m}$ and width: 0.6 $\mu\text{m}$ (faceted)	$(0001)_{Mg} \wedge (0001)_{Zr}$ and $[2\bar{1}\bar{1}0]_{Mg} \parallel [2\bar{1}\bar{1}0]_{Zr}$	$\sim 28^\circ$	11.1%	no
0.5 $\mu\text{m}$ (faceted)	$(11\bar{2}2)_{Mg} \wedge (11\bar{2}2)_{Zr}$ and $[\bar{1}2\bar{1}3]_{Mg} \parallel [\bar{1}2\bar{1}3]_{Zr}$	$\sim 1^\circ$	0.13%	yes
0.6 $\mu\text{m}$ (faceted)	$(0001)_{Mg} \wedge (0001)_{Zr}$ of lattice fringes	$\sim 30^\circ$	12.9%	no

## 5.4 Conclusion

It is shown that TEM with SADP or HRTEM is an excellent tool for identifying particles that are likely nucleation sites. The TEM study from the magnesium-0.5% zirconium (pouring temperature = 815°C, and settling time = 30 min) grain refined sample showed that a range of zirconium particles (0.23-1.6  $\mu\text{m}$ ) act as nucleation sites. This supports Greer's free growth theory that different nucleating substrates will become active when the required undercooling is achieved. Table 5.1 shows the detail compilation of all the zirconium particles observed under TEM. Likely nucleation sites, i.e. particles that show parallel axis orientation relationship with small planar disregistry ( $\sim 0.1$ - $0.2\%$ ) appear to be faceted. This is reasonable as zirconium particles which are faceted in nature are likely to expose a suitable nucleating substrate to the matrix. The orientation relationship (OR) between the nucleus and the matrix suggests that mainly  $(0001)_{\text{Mg}} \parallel (0001)_{\text{Zr}}$  and  $(10\bar{1}0)_{\text{Mg}} \parallel (10\bar{1}0)_{\text{Zr}}$  are parallel indicating that the basal plane  $\{0001\}$  and the prismatic plane  $\{1010\}$  of zirconium particles are likely suitable sites for heterogeneous nucleation. The TEM investigation also shows that zirconium particles which are likely not nuclei will have a large angle of misorientation with the matrix. HRTEM of the particle-matrix interface shows that magnesium grows epitaxially on a suitable plane of zirconium. Particles which are not nucleation sites show dislocation or atomic misfit at the particle-matrix interface and a large planar lattice disregistry.

## 6. DISSOLUTION STUDY: PARTICLE MORPHOLOGY, AND SIZE DISTRIBUTION

### 6.1 Introduction

In alloy casting it is desirable for the grain structure to be fine and equiaxed. Grain refinement is a universal method by which the liquid melt is inoculated with heterogeneous nucleation particles to improve the quality of the casting performance and mechanical properties of common foundry alloys [4, 43]. For aluminum alloy industry the most widely used and known inoculants are Al-Ti-B type master alloy [44]. The addition of master alloy to the melt resulted immediate dissolve of the  $AlTi_3$  particles in the melt [4] and increase the soluble titanium level in the melt which serves as growth restrictor of  $\alpha$ -aluminum grains nucleated on suitable  $TiB_2$  particles [11] available in the melt. However, it was observed approximately 1%  $TiB_2$  particles act as nucleating center for the growing grain [18, 45]. The inefficiency of the commercial grain refiners increase the cost of production as higher amount of refiner needed to add to get the optimum grain refinement. It also affects the resultant microstructures of the solidified alloy. Davies *et al.* [46] found active particles at the center of a grain and show a preferred orientation relationship with the surrounding matrix whereas inactive particles pushed to the grain boundary where they have pushed to in front of the solid-liquid interface. Maxwell and Hellawell's hypothesized [16] that the final grain size is a result of competition between heterogeneous nucleation and crystal growth and there is a detectable small recalescence caused by the release

of latent heat from the growing crystals stifles further nucleation events. Recently, Greer et al. [18] developed a free growth model to predict the as-cast grain size in aluminum casting alloys. The main attribute of Greer's model was grain formation is growth limited rather than nucleation limited. Greer *et al.* [36] also observed the barrier of nucleation is very small (0.15 K) for all the effective nucleants present in the melt. The good agreement of their predictions with the experimental results indicated that particles which are large enough in size effectively inoculate the metals. This sort of particles is called active nucleation particles. However, the effect of the active nucleation particles on grain refinement efficiency has not been fully addressed previously.

In the recent past extensive research has been focused on developing new grain refiner for magnesium cast alloys, and a number of grain refiners have been reported, such as zirconium for magnesium alloys which do not contain elements such as aluminum, manganese and silicon, since zirconium forms stable compounds with these elements [5] and  $\text{Al}_4\text{C}_3$  [47, 48],  $\text{SiC}$  [49, 50] or by carbon inoculation [51, 52] for aluminum bearing magnesium alloy. Although the dependence of grain refining efficiency at different addition level of inoculated particles has been investigated [53, 54] there is still lack of experimental data on the role of the active particles in grain refinement. Qian et al [55] reported that not all the zirconium particles contribute to the grain refinement in pure magnesium and the active zirconium particle size is around 2  $\mu\text{m}$  however, there is no experimental evidence show the efficiency of the grain refiner used at different experimental condition. Easton and StJohn [56, 57] reported a semi-empirical model to predict the final grain size of the as-cast aluminum. The grain size  $d$  was defined as

$$d = \frac{1}{\sqrt[3]{f\rho}} + \frac{b_1\Delta T_n}{Q} \quad (6.1)$$

where,  $\rho$  is the number density of particles present in the melt and  $f$  is the fraction of these particles that are active nucleant for the formation of grains,  $b_1$  is a fitting factor;  $\Delta T_n$  is the nucleation undercooling and  $Q$  growth restriction factor. They also fitted the experimental data of the grain size for an aluminum alloy grain refined with Al-3Ti-1B master alloy with their semi-empirical model [58].

In the present work the size distributions of zirconium particles were determined from the grain refined samples. Dissolution samples were analyzed by SEM to determine the particle morphology (size and shape) and different grain refined samples were compared with each other. The data provides an insight into the total number of faceted particles present in samples cast under various conditions. Based on this information, a relationship was established between the number density of particles for each grain refined sample and compared with the grain density to determine the efficiency of zirconium particles nucleating a grain. The efficiency of faceted particles was also compared.

## **6.2 Particle Size and Morphology**

The dissolution samples were used for two purposes:

1. Determine the particle size distribution, and
2. Count the number of faceted particles present in each sample.

Samples were dissolved into 1% diluted hydrochloric acid (0.1 g/10 ml basis). The solution was kept for 72 hrs to digest the sample completely. After the samples were dissolved completely, 1 ml of the solution was transferred in a EPPENDORF tube and centrifuged at 15000 r.p.m. for 15 min in 3 cycles. After each cycle the liquid was decanted and de-ionized water was added to the mixture. This allowed magnesium chloride, which is highly soluble in

water, to be washed away and for the zirconium particles to be collected at the bottom. At the end of each cycle the tube was sonicated for 10 min.

### *6.2.1 Measurement of Particle Size and Distribution*

The final centrifuged sample was ultra-sonicated for 30 min and one drop of the solution was evenly distributed on a silicon wafer. The wafer was dried and kept under vacuum to prevent it from being contaminated. The silicon wafer with the zirconium particles was characterized by SEM at an accelerating voltage of 15 kV, working distance of 10 mm and spot size of 7 nm.

The zirconium particle size was determined using the Accusizer model 770 particle size analyzer that uses the light obscuration/photozone method. The work was performed by Particle Technology Laboratory, *PTL*<sup>®</sup>, Illinois, USA. A 1ml of centrifuged sample from the grain refined samples was diluted to avoid exceeding coincidence (more than one particle passing through the zone simultaneously). A 60 ml sample of the liquid was passed through different channels (total 128) for 60 s and each channel counted the number of particles and size were determined by an optical laser sensor (photo sensing zone).

### *6.2.2 Measurement of Faceted Particle Density*

SEM micrographs of the zirconium particles obtained from the dissolution studies reveal that different sizes and shapes of zirconium particles are present in the grain refined sample. Earlier TEM observation of the grain refined samples suggested that only faceted zirconium particles are suitable nucleation sites for magnesium grains. Faceted zirconium particles evident from the SEM micrographs from each grain refined sample were counted to give an indication of

- the number of faceted particles present, and
- faceted particle density in each grain refined sample.

Each SEM micrograph (Fig. 6.3) obtained from the dissolution studies for each grain refined samples was first calibrated with NIKON NIS-Elements image analysis software. Next, zirconium particles were detected using the automated thresholding picking tool. Zirconium particles which show a clear facet and did not have any rounded and curved surface were designated and counted as faceted particles (outlined with a green line). The total particles were counted by picking each particles with an automatic counting tool.

### **6.3 Results of Particle Size Distributions of Grain Refined Samples**

An Accusizer model 770 (Particle Technology Laboratory, *PTL*<sup>®</sup>, Illinois, USA) was used to determine the population distribution of particles present in grain refined samples. The instrument was only capable of measuring particles greater than 0.5  $\mu\text{m}$ . To enable the comparison of the number distribution of zirconium particles in different samples, only particle sizes ranging between 0.5 and 5  $\mu\text{m}$  are plotted. The particle size analysis data showed that particles greater than 5  $\mu\text{m}$  were present in extremely small numbers. Fig. 6.1 shows the number of particles present in the magnesium-0.25% zirconium grain refined sample at 0 and 30 min. It is observed that the 0 min sample exhibits a wide size distribution and a large number of particles (total count was 83,212 in 1 ml of the dissolution sample) while the 30 min sample has a narrow distribution and a drastically smaller number of particles (total count was 6170 in 1 ml of the dissolution sample). Section 4.3 it was shown that at 30 min particles greater than 2  $\mu\text{m}$  will settle at least 20 mm. While it might be expected that large particles will settle and be unavailable for grain refinement, the drastic decrease in particles smaller than 2  $\mu\text{m}$  suggests that smaller particles likely coalesced and settled, providing a far smaller particle counts than expected. The phenomena of particle settling and a consequent increase in grain size is commonly observed during industrial practice and is termed fading.

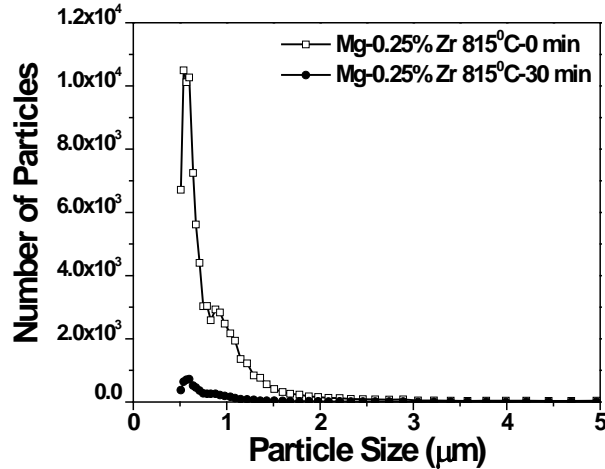


Fig. 6.1 Particle size distribution of zirconium particles present in magnesium-0.25% zirconium grain refined samples at 0 and 30 min determined using a light obscuration/photozone method. The drastically lower number of particles at 30 min suggests fading, particle agglomeration and settling with time.

A similar trend was also observed in the magnesium-1% zirconium sample and is shown in Fig. 6.2. However, the total numbers of particles were relatively high compared to the magnesium-0.25% zirconium sample. This explains why the increase in grain size is much smaller at 30 min at the 1% zirconium level compared to 0.25% zirconium.

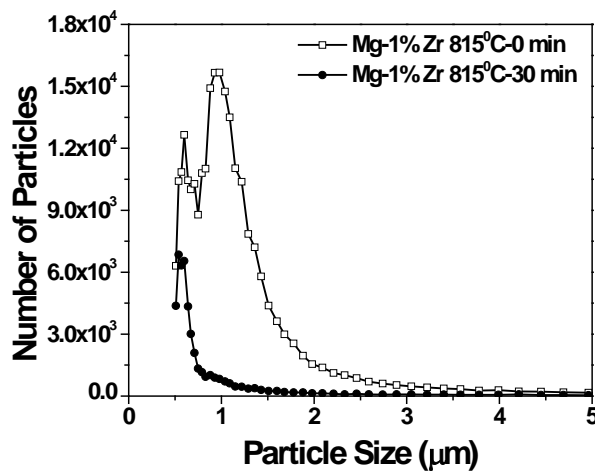


Fig. 6.2 Particle size distribution of total number of zirconium particles available in magnesium-1.0% zirconium grain refined samples at different settling time determined from light obscuration/photozone method. Total number of particles in the diameter range 0.5-5  $\mu\text{m}$  was calculated as 244,429 and 45,377 in 1 ml of the dissolution sample in 0 min and 30 min sample respectively.

Table 6.1 shows the particle distribution (%) in the 0.25 wt% and 1wt% grain refined samples. An interesting observation is that the majority of the particles are in the range of 0.5 to 2  $\mu\text{m}$ . This suggests that particles that result in grain refinement are also likely to be in the range (Note: This was largely supported by the TEM investigations outline in Chapter 5). Another interesting observation is that except in the case of magnesium-1 wt% zirconium, 0 min sample, the particle size distribution is almost identical. Couple with the particle size distribution data in Fig. 6.1 and 6.2, it appears that the variation in grain size is due to the number of particles available, rather than the particle size distribution.

TABLE 6.1 Particle size distributions (%) in the 0.25 wt% and 1 wt% grain refined samples

Particle size range ( $\mu\text{m}$ )	Mg-0.25 wt% Zr 815°C/0 min (%)	Mg-0.25 wt% Zr 815°C/30 min (%)	Mg-1 wt% Zr 815°C/0 min (%)	Mg-1 wt% Zr 815°C/30 min (%)
< 1 $\mu\text{m}$	85.79	81.84	59.94	84.82
> 1-2 $\mu\text{m}$ <	12.43	12.16	35.52	9.45
> 2-3 $\mu\text{m}$ <	0.81	1.38	2.52	1.43
> 3-4 $\mu\text{m}$ <	0.31	0.63	0.87	0.87
> 4-5 $\mu\text{m}$ <	0.18	0.45	0.32	0.46
> 5 $\mu\text{m}$	0.48	3.08	0.82	2.97
mean ( $\mu\text{m}$ )	0.81	1.18	1.09	1.1
median ( $\mu\text{m}$ )	0.64	0.67	0.93	0.6
STD	0.94	2.46	1.02	2.24
Total counts	83,614	6377	246,461	46,765

#### 6.4 Nucleant Particle Efficiency

The fraction of zirconium particles responsible for nucleating grains in each grain refined sample was calculated. It was assumed that the total particle density ( $\text{mm}^{-3}$ ),  $N_v^P$  was equal to the number of particles present at the start of the melt, i.e., the particle density for the 0 min sample. The next

step was to estimate the grain density. This was accomplished using the formula given by Greer

$$et al. [18] \text{ i.e., } N_v^G = \frac{0.5}{\bar{l}^3}$$

where,  $N_v^G$  = grain density, and

$\bar{l}$  = mean lineal intercept of grains.

The nucleant particle efficiency was calculated as the ratio of the grain density to the total particle density. This assumes that each nucleant particle only nucleates a single grain. Table 6.2 lists the grain size, grain density, total particle density, and the nucleant particle efficiency for the magnesium-0.25 wt% and 1 wt% zirconium grain refined samples.

It is clearly seen that the fraction of active zirconium particles decreases with increasing settling time. Importantly, in all cases, the fraction of active zirconium particles is less than 2% suggesting that only a few of the total particles take part in grain refinement. Greer *et al.* [18] found that the nucleant particle efficiency of TiB<sub>2</sub> particles added from a TiBor grain refiner to aluminum melts was similar.

Table 6.2 Comparison of nucleation efficiency of total zirconium particles in different grain refined samples

Sample ID	Grain size (μm)	Grain density (mm <sup>-3</sup> ) ( $N_v^G$ )	Total Particle density (mm <sup>-3</sup> ) ( $N_v^p$ )	Nucleant particle efficiency (%)
Mg-0.25 wt% Zr 815°C-0 min	109	386	56987	<b>0.68</b>
Mg-0.25 wt% Zr 815°C-30 min	230	41	56987	<b>0.07</b>
Mg-1 wt% Zr 815°C-0 min	51	3769	266667	<b>1.41</b>
Mg-1 wt% Zr 815°C-30 min	60	2315	266667	<b>0.87</b>

## 6.5 Grain Density vs. Faceted Particles Density

Fig. 6.3 shows SEM micrographs of the dissolution samples for 0.25 and 1wt% zirconium additions. The SEM micrographs clearly reveal that different sizes and shapes of particles are present in the grain refined sample. The numbers and sizes of faceted particles were counted from each sample and used to calculate the nucleation efficiency of the faceted particles.

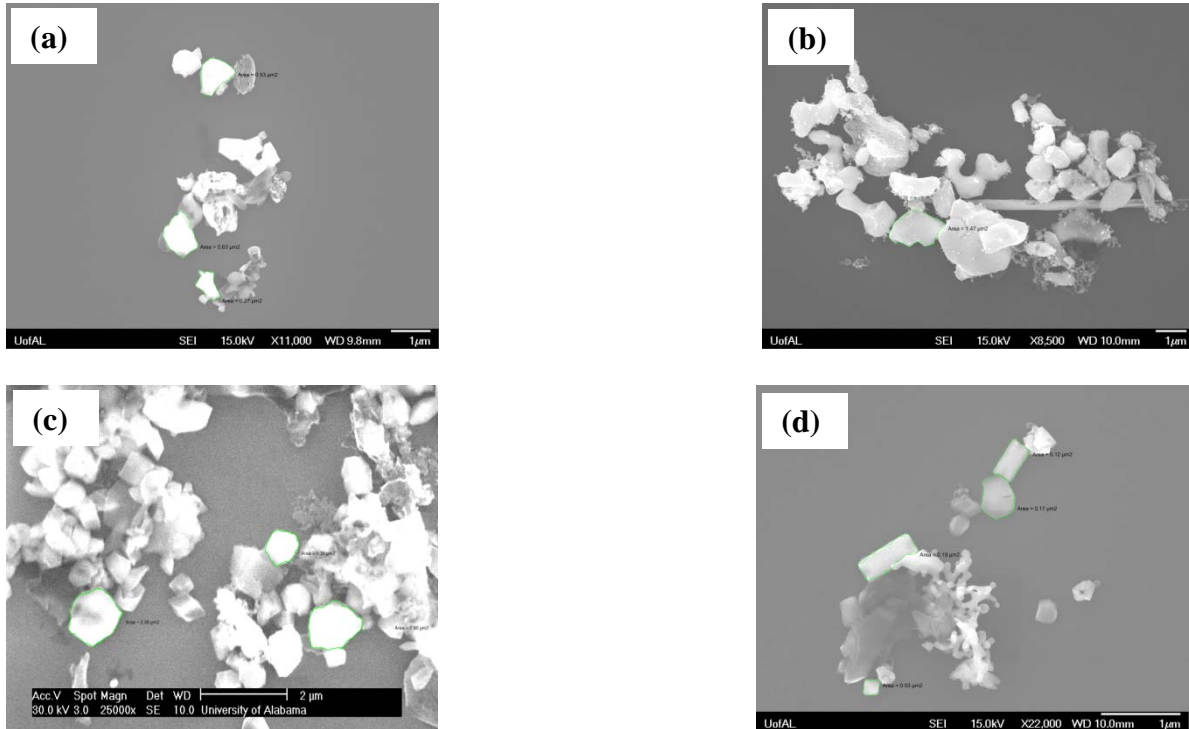


Fig. 6.3 SEM micrographs of zirconium particles observed from the dissolution study at 0 min (a) magnesium-0.25 wt% zirconium, (b) magnesium-1 wt% zirconium; and 30 min (c) magnesium-0.25 wt% zirconium, (d) magnesium-1 wt% zirconium grain refined samples.

Table 6.3 shows a comparison of the number of faceted particles observed in the SEM micrographs for each grain refined sample. It is observed that approximately 2 to 5% faceted particles are present in each grain refined sample. Table 6.3 also shows that the percent of faceted particles increased with 30 min of settling time. The increase in the number of faceted particles at 30 min might be due to the fact that the particles dissolved partially and exposed facets in the melt.

Table 6.3 Fraction of faceted zirconium particles present in different grain refined samples

Sample ID	Number of total particles	Number of faceted particles	Fraction of faceted particles (%)
Mg-0.25 wt% Zr 815°C-0 min	599	15	<b>2.5</b>
Mg-0.25 wt% Zr 815°C-30 min	628	33	<b>5.3</b>
Mg-1 wt% Zr 815°C-0 min	354	8	<b>2.3</b>
Mg-1 wt% Zr 815°C-30 min	348	16	<b>4.6</b>

Table 6.4 show a comparison of the grain density with faceted particle density. It is evident that nucleation efficiency of the faceted particles show excellent match with the grain density. This result suggests that only faceted particles were only active nucleation sites for magnesium grains

Table 6.4 Comparison of nucleation efficiency of faceted zirconium particles in different grain refined samples

Sample ID	Grain size ( $\mu\text{m}$ )	Grain density ( $\text{mm}^{-3}$ ) ( $N_v^G$ )	Faceted particle density ( $\text{mm}^{-3}$ ) ( $N_v^F$ )	Faceted particle efficiency (%)
Mg-0.25 wt% Zr 815°C-0 min	109	386	952	<b>40.5</b>
Mg-0.25 wt% Zr 815°C-30 min	230	41	114	<b>36.0</b>
Mg-1 wt% Zr 815°C-0 min	51	3769	5973	<b>63.1</b>
Mg-1 wt% Zr 815°C-30 min	60	2315	6029	<b>38.4</b>

Since only faceted particles appear to become nucleation sites, and the number of faceted particles doubles after 30 min, it was decided to test this effect with the following experiments.

Previous grain refinement experiments only cast hockey pucks at 0 and 30 min. The remaining melt was usually discarded. For this test, the melt remaining at 30 min for 2 wt% zirconium-705°C pouring temperature sample was vigorously stirred and poured to form a hockey puck sample. Fig. 6.4 shows the optical micrographs obtained from the above experiments. Remarkably the grains size for the restirred sample (Fig. 6.4(c)) is only 22  $\mu\text{m}$ , compared to 55  $\mu\text{m}$  for the 0 min sample (Fig.6.4 (a)), and 82  $\mu\text{m}$  for the 30 min sample (Fig. 6.4(b). The tremendous decrease in the grain size from 30 min to 30 min-restirred sample is likely due to the fact that faceted particles increase with increasing settling time.

## 6.6 Conclusion

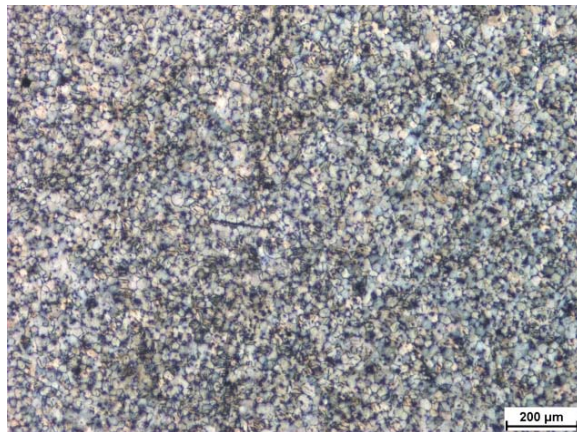
The dissolution study of grain refined samples suggests that due to the settling of particles (fading) far few particles are present at 30 min grain refined samples compared to 0 min. The reduction in the number of particles at 30 min explains the substantially larger grain size in the 30 min grain refined samples. The dissolution study of the grain refined samples showed that more faceted particles were present in the 30 min sample. It is likely that particles partially dissolved and exposed facet in the melt. A comparison of grain density with total particle density suggests less than 2% of the particles are active nucleation centers. However, a similar comparison with faceted particles shows that 36 to 63% of faceted particles are active as nucleation centers for magnesium grains. This suggests that only faceted particles are the active nucleation centers. It was also shown that stirring the melt after 30 min had a dramatic improvement in the overall grain refinement. This further proves that only faceted particles are nucleation sites as the number of faceted particles doubles after 30 min in contact with the melt.



(a) 55  $\mu\text{m}$



(b) 82  $\mu\text{m}$



(c) 22  $\mu\text{m}$

Fig. 6.4 Optical micrographs of samples poured at 705°C at a) 0 min settling time, b) 30 min settling time and (c) 30 min-restirred sample The measured grain size is indicated below of each micrograph (magnifications 50x).

## 7. ENGINEERING A MORE EFFICIENT ZIRCONIUM-BASED GRAIN REFINER

### 7.1 Introduction

As shown in Fig. 7.1, the magnesium-15 wt% zirconium master alloy used for this work contains large particles and particle clusters that are detrimental to mechanical properties. Allowing the melt to settle results in a large decrease in the number of particles available (Fig. 6.1 and 6.2).

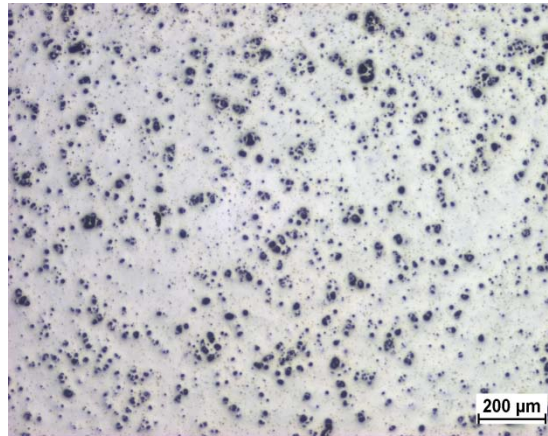


Fig. 7.1 Optical micrograph in the unetched condition for magnesium-1.0 wt% zirconium sample poured at 815°C, 0 min.

Also, the analysis in Chapter 6 showed that only faceted particles are responsible for grain refinement. Accordingly, the goal of this task was to increase the grain refinement efficiency of the original master alloy by increasing the total number of faceted particles. The original master alloy was subjected to severe plastic deformation at an elevated temperature by the Equal Channel Angular Extrusion (ECAE) process to break up the large zirconium particles and particle clusters. Fig. 7.2 is a SEM micrograph of the original master alloy showing

a large particle clusters.

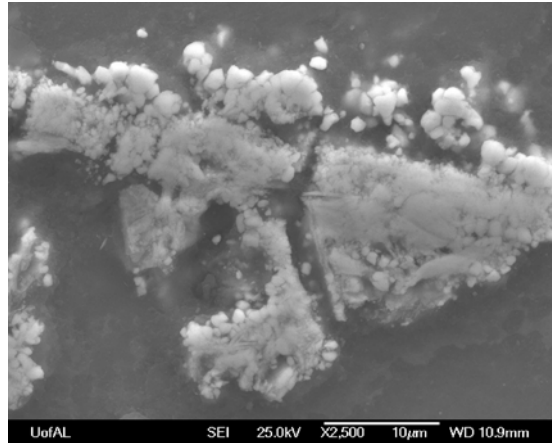


Fig. 7.2 SEM micrograph of the magnesium-15wt% zirconium master alloy show zirconium particle and particle clusters greater than 5  $\mu\text{m}$  along the grain boundary.

## 7.2 ECAE Process

The ECAE process is based on intensive material deformation by repeated simple shear. The ECAE process incorporates large strains without requiring a change in the original work piece

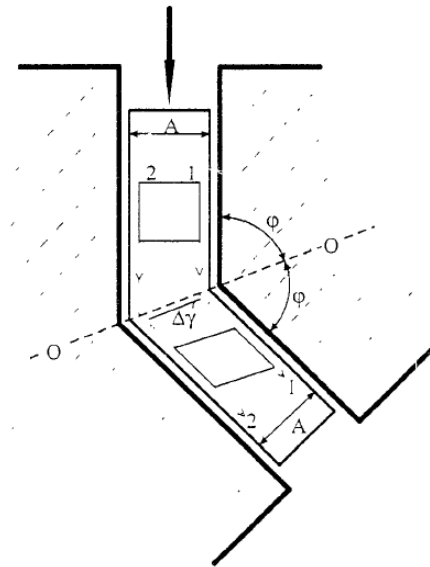


Fig. 7.3 A schematic diagram of the ECAE process. The extrusion direction is illustrated by flow lines 1-1 and 2-2. Deformation is achieved by simple shear along the crossing plane (00) of the channel [59].

cross-section. The process involves the extrusion of a well lubricated billet through two intersecting channels of identical cross-section. Deformation is achieved by simple shear along the intersecting plane of the two channels [59]. Fig. 7.3 shows a schematic diagram of ECAE process.

### 7.3 ECAE Processing of the Original Magnesium-15 wt% Zirconium Master Alloy

Rods 12 mm in diameter and 75 mm in length were machined from the magnesium-15 wt% zirconium master alloy. One rod sample was encapsulated in a steel can as shown in Fig. 7.4 and deformed by ECAE route 4A, (i.e. 4 passes with no rotation between multiple passes) at 300°C.



Fig. 7.4 Photograph of magnesium-15 wt% zirconium ECAE processed billet encapsulated in steel can.

The ECAE process spreads out grain boundaries (i.e., elongates the grains as if the material were rolled) and therefore disperses the zirconium particles over a larger volume [59]. For the square billet in this work, the flow plane was designated as the side plane as it exits the ECAE die. The longitudinal plane was the top of the billet as it exits the die, and the transverse plane was the plane perpendicular to the long axis of the billet (see. Fig.7.5). The flow plane

view of the deformed billet determines how well the ECAE processing worked for the processing conditions used.

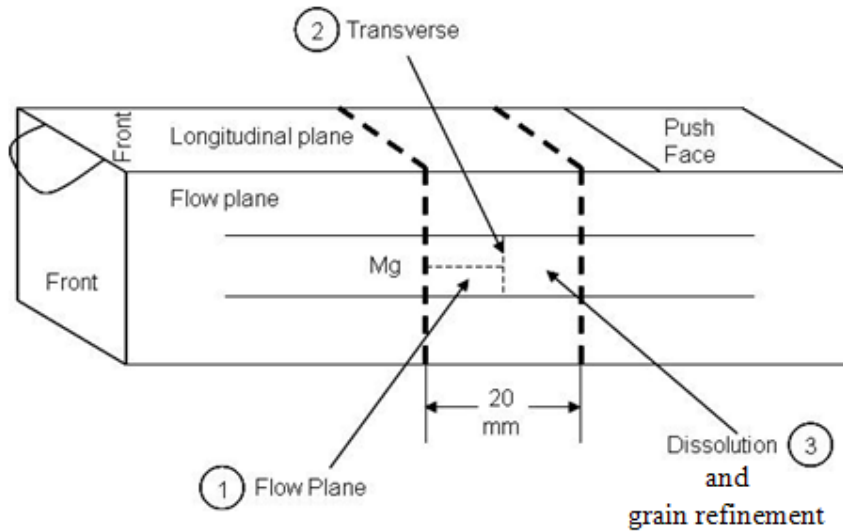


Fig. 7.5 Schematic diagram of the magnesium-15 wt% zirconium ECAE processed billet showing the flow plane or the side plane of the billet, the longitudinal plane the top plane of the billet, the transverse plane, i.e. the plane perpendicular to the long axis of the billet, and the push face of the billet.

#### 7.4 Microstructural Characterization of the ECAE Processed Billet

The ECAE processed billet was sectioned into three pieces as shown in Fig. 7.5. The center piece was selected for microstructural analysis, dissolution and grain refinement study.

Fig. 7.6 shows a comparison of the microstructure of the original master alloy and the ECAE processed billet. The microstructure of the original magnesium -15wt% zirconium master alloy (Fig. 7.6a and b) contains large zirconium particles along the grain boundary. After ECAE processing, the grains become elongated and the particles are spread along grain boundaries (Fig. 7.6c). The large zirconium particles and particle clusters which were originally at the grain boundary are sheared over a large volume and broken into small individual particles (Fig. 7.6d).

The micrographs in Fig. 7.6 suggest that ECAE was an effective method to break up the zirconium particles and particle clusters.

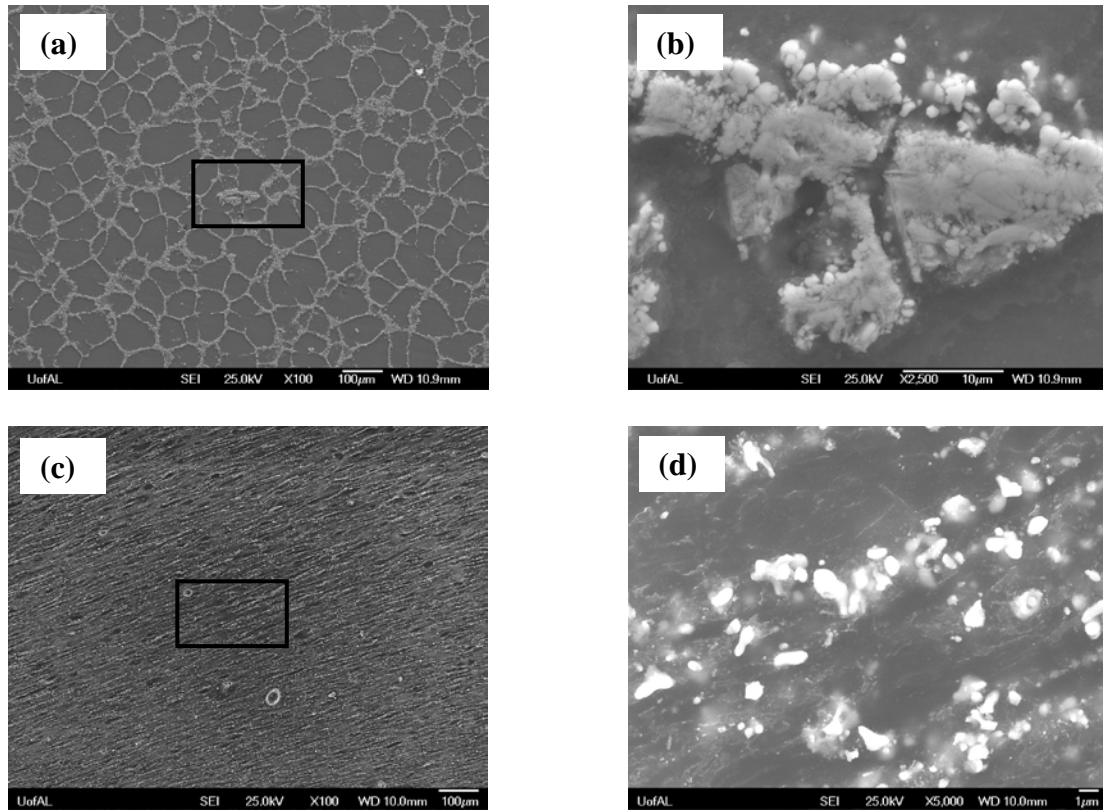


Fig. 7.6 (a) Scanning electron micrograph showing large zirconium particles and particle clusters along the grain boundary in magnesium-15 wt% zirconium master alloy, (b) enlarged view of the small marked region in (a) showing large particle clusters; (c) Scanning electron micrograph of the ECAE processed magnesium-15wt% zirconium used for the work (d) enlarged view of the small marked region in (a) showing small and large number of zirconium particle. ECAE helped to break up the particle cluster and spread over large volume.

### 7.5 Dissolution Study of the ECAE Processed and the Original Master Alloys

The original master alloy and the ECAE processed alloy were dissolved into 1% dilute hydrochloric acid (0.1 g/10 ml basis). The dissolution sample was prepared according to the methodology outlined in Section 6.2. The dissolution samples were used for two purposes:

1. Determine the particle size distribution, and
2. Count the number of faceted particles present in each sample.

### 7.5.1 Particle Size Distribution of the ECAE Processed and the Original Master Alloys

Fig. 7.7 shows the particle size distribution of the original and the ECAE processed master alloy. It is apparent that ECAE processing increases the number of particles and narrows the size distribution. It is also apparent that the number of small particles (0.5-2  $\mu\text{m}$ ) increased in the ECAE processed alloy.

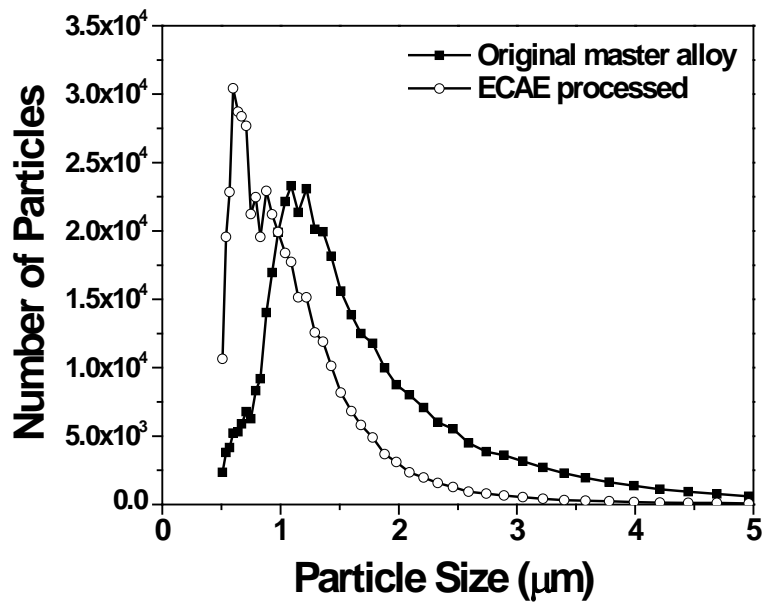


Fig. 7.7 Particle size distribution of original master alloy and ECAE processed master alloy determined using the light obscuration/photozone method. The total number of particles in the diameter range of 0.5-5  $\mu\text{m}$  was measured to be 383,866 in the original master alloy and 441,055 in the ECAE processed sample.

Table 7.1 show a comparison of the particle size distribution obtained using the Accusizer Model 770 (Particle Technology Laboratory, *PTL*<sup>®</sup>, Illinois, USA). In the ECAE processed alloy, approximately 68% of the particles are between 0.5 and 1  $\mu\text{m}$  in size, whereas in the original master alloy, only 28% particles were between 0.5 and 1  $\mu\text{m}$  in size.

Table 7.1 Particle Size Distributions for the Original and ECAE Processed Master Alloys

Particle size range ( $\mu\text{m}$ )	Original Master Alloy (%)	ECAE Processed (%)
> 0.5 -1 $\mu\text{m}$ <	27.97	66.94
> 1-2 $\mu\text{m}$ <	57.06	30.23
> 2-3 $\mu\text{m}$ <	9.98	2.16
> 3-4 $\mu\text{m}$ <	3.39	0.45
> 4-5 $\mu\text{m}$ <	0.89	0.11
> 5 $\mu\text{m}$	0.71	0.11
mean ( $\mu\text{m}$ )	1.46	0.96
Total counts	386,611	441,526

7.5.2 Faceted Particles in the ECAE Processed and Original Master Alloy

Fig. 7.8 shows SEM micrographs of the ECAE and original master alloy dissolution samples. It is apparent that different shapes and sizes of zirconium particles were present in the original master alloy but the majority of the particles in the ECAE processed master alloy appear to be regular and in the submicron to 2  $\mu\text{m}$  range. Faceted particles were counted from SEM micrographs and compared with the total number of particles in the micrographs.

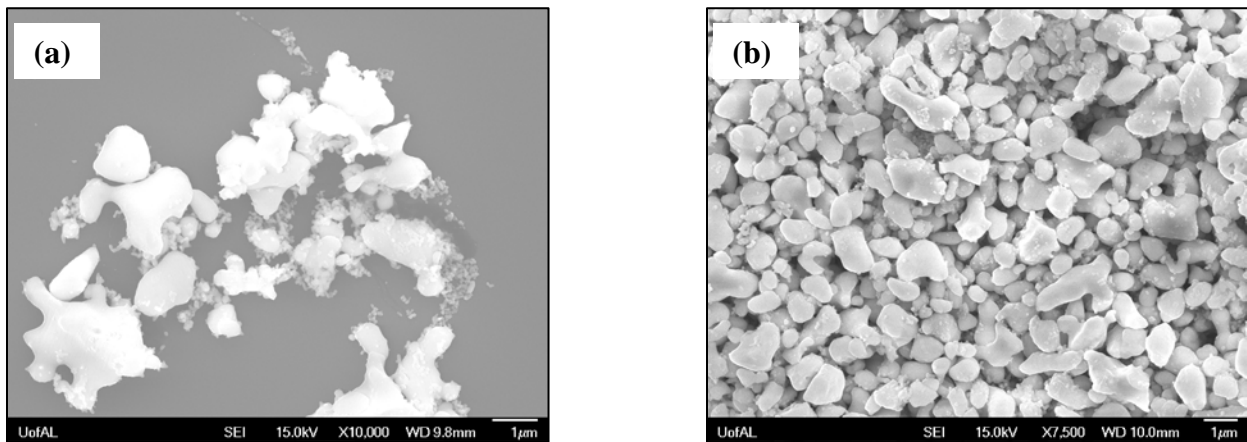


Fig. 7.8 SEM micrographs of zirconium particles observed from the dissolution study (a) original master alloy, and (b) ECAE processed master alloy.

It was found that 1.58% of faceted particles were present in the original master alloy, whereas 3.31% of faceted particles were present in the ECAE processed sample. The increase in the number of faceted particles suggests that ECAE broke up the large particles and created more faceted particles.

Fig. 7.9 shows the number and size distribution of the faceted particles obtained from the dissolution study of the original and ECAE processed master alloys. In the original master alloy, faceted particles were present in a wide distribution of 0.5 to 2.5  $\mu\text{m}$ , with almost equal number of faceted particles present in each size range.

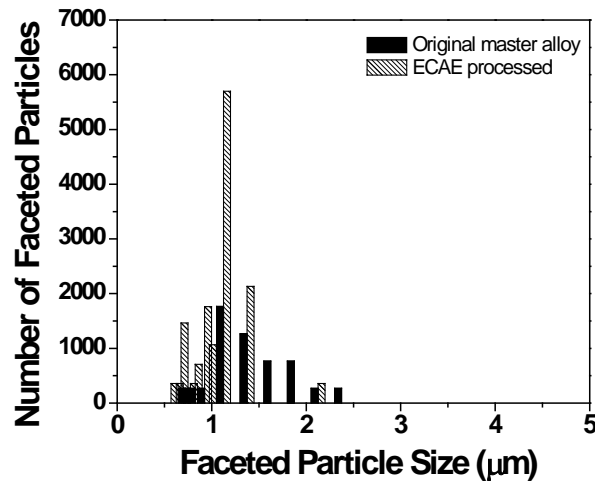


Fig. 7.9 Particle size distribution of faceted zirconium particles observed in the original master alloy and ECAE processed samples.

In case of the ECAE processed master alloy, a narrow size distribution of particles was observed and a significant number of particles were in the 1  $\mu\text{m}$  range. Table 7.1 shows that ECAE broke up the zirconium particles and majority of the particles were within 0.5 to 2  $\mu\text{m}$  size (97%). The number of the faceted particles show that approximately 40% of the faceted particles were between 1-1.25  $\mu\text{m}$  in the ECAE processed sample. ECAE not only increased the number of faceted particle but also the size of those particles were within desired particle size range.

## 7.6 Grain Refinement Experiments with ECAE Processed Master Alloy

Grain refinement experiments were conducted with the original and ECAE processed master alloys. Since an important goal of this work was to significantly reduce the amount of zirconium used, 0.1 wt% zirconium was added to pure magnesium and a hockey puck sample was poured at 815°C and 0 min. Neither the original master nor the ECAE processed master alloy produced any grain refinement at the 0.1% zirconium level. Fig. 7.10 shows an optical micrograph of the sample poured at 815°C and 0 min with 0.1% zirconium from the ECAE processed alloy.

It became immediately apparent that at the 0.1% zirconium level, there was insufficient solute in the melt. Inductive Couple Plasma Atomic Emission Spectroscopy (ICP-AES) was performed to determine the soluble zirconium in the melt, and showed that only 0.02% soluble zirconium was available in the melt. This low amount of solute was not sufficient for grain refinement. To counter the problem of insufficient solute, 2 wt% of zinc was added to the melt. Zinc was chosen as it was compatible with zirconium and was not reported to poison the grain refinement ability of zirconium.



667 μm

Fig. 7.10 Optical micrographs of magnesium-0.1 wt% zirconium sample poured at 815°C 0 min settling time indicate no grain refinement. The measured grain size is indicated below the micrograph (magnifications 50x).

### 7.6.1 Experimental Method

Grain refinement experiments were conducted with additions of 2 wt% zinc and 0.05% and 0.1 wt% zirconium from the ECAE processed and original master alloys. Hockey puck samples were poured for all the four samples at 815°C and 0 min. The melting and casting procedure used was identical to that for previous hockey pucks except that once the melt reached temperature, 2 wt% zinc was added and the melt was stirred vigorously for 15 s. The zinc was allowed to dissolve and equilibrate for 2 min, after which the melt was skimmed of any oxide and then the grain refiner was added.

A separate experiment was also performed with magnesium-2 wt% zinc to check whether the addition of zinc by itself had any effect on the grain refinement or not. Fig. 7.11 shows an optical micrograph obtained from the magnesium-2 wt% zinc sample. The measured grain size was 476  $\mu\text{m}$ , showing that there was no grain refinement.

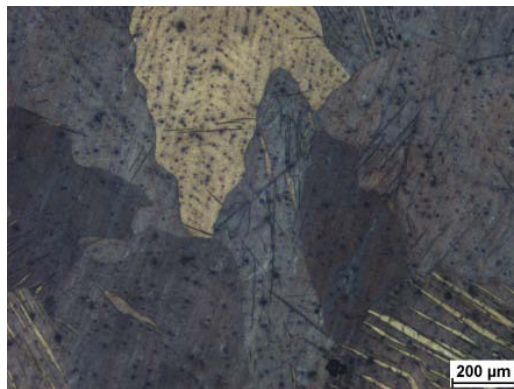


Fig. 7.11 Optical micrographs of magnesium-2 wt% zinc sample poured at 815°C, 0 min indicating no grain refinement. The measured grain size was 476  $\mu\text{m}$  (magnification 50x).

Fig. 7.12 shows the optical micrographs obtained from the magnesium-2 wt% zinc-0.05 and 0.1 wt% zirconium experiments. It is clear that the ECAE processed master alloy had a significant improvement on the overall grain refinement. The improvement in grain refinement

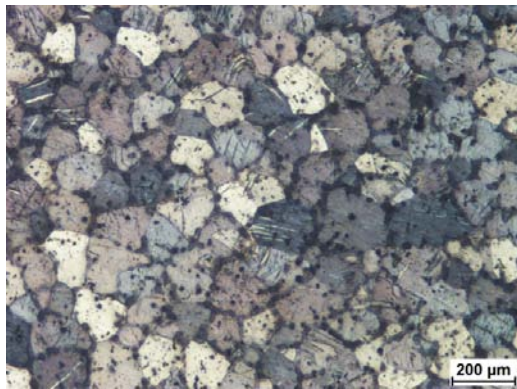
behavior of the ECAE processed master alloy is attributed to the increase in the number of faceted particles in the sample. This is particularly evident in the case of the 0.05% zirconium addition, since due to the small number of particles available at 0.05% zirconium, the increased number of faceted particles in the ECAE processed alloy made a noticeable difference. The above results corroborate and confirm that the hypothesis advanced in Chapter 6 that only faceted particles are active nucleation centers.



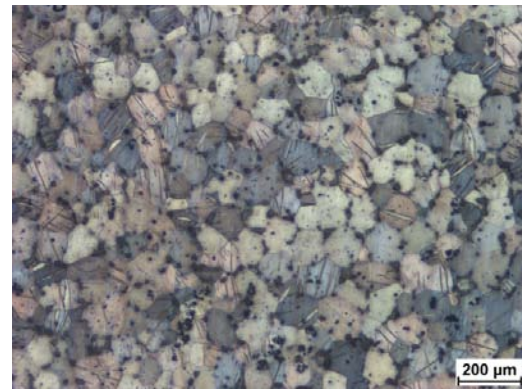
(a) 385  $\mu\text{m}$



(b) 270  $\mu\text{m}$



(a) 131  $\mu\text{m}$



(d) 270  $\mu\text{m}$

Fig. 7.12 Optical micrographs of magnesium-2 wt% zinc-0.05 wt% zirconium sample poured at 815°C, 0 min (a) using original master alloy indicate no grain refinement, and (b) using ECAE processed master alloy indicate significant grain refinement. For magnesium-2 wt% zinc-0.1 wt% zirconium sample poured at 815°C, 0 min (c) using original master alloy showing grain refinement and (d) using ECAE processed master alloy showing measurable improvement in grain refinement. The measured grain size is indicated below the micrographs (magnification 50x).

## 7. CONCLUSION

A systematic DOE study of the grain refinement of magnesium by zirconium shows that the peritectic reaction is not needed for grain refinement. This provides an opportunity for the development of a more efficient grain refiner, i.e. usage of zirconium far less than the 1 wt% used currently.

TEM with SADP or HRTEM is an excellent tool for identifying particles that are likely nucleation sites. Likely nucleation sites are faceted particles that show a parallel axis orientation relationship and small planar disregistry ( $\sim 0.1$  to  $0.2$ ) with the matrix.

TEM analysis of the 0.5 wt% Zr-815°C-30 min grain refined sample showed that a range of zirconium particles ( $0.23$  to  $1.6 \mu\text{m}$ ) which can act as nucleation sites. This can be explained by Greer's free growth theory that a range (of size) of particles will become active nucleation centers when the required undercooling is achieved.

A comparison of grain density with total particle density suggested that less than 2% of the particles are active nucleation centers. However, grain density shows close and excellent agreement with faceted particle density, suggesting that only faceted particles are likely nucleation sites. Experimental evidence of the efficacy of faceted particles in grain refinement is provided in the dramatic reduction in grain size achieved ( $22 \mu\text{m}$ ) when the melt is restirred prior to casting after 30 min, since the number of faceted particles increases substantially with holding time.

The ECAE processed master alloy provided significant improvement in grain refinement over the original master alloy. Improvement in grain refinement behavior of the ECAE processed alloy is attributed to the increase in the number of faceted particles i.e. 3.31% in the ECAE processed alloy compared to only 1.58% in the original master alloy.

The above results show that there is a tremendous opportunity to improve the performance of current grain refiners.

## REFERENCES

- [1] F. Froes, D. Eliezer, and E. Aghion, "The science, technology, and applications of magnesium," *JOM Journal of the Minerals, Metals and Materials Society*, vol. 50, pp. 30-34, 1998.
- [2] Q. T. Fang and D. A. Granger, "Porosity Formation in Modified and Unmodified A356 Alloy Casting," *AFS Transaction*, vol. 97, pp. 989-1000, 1989.
- [3] G. Chai, L. BÄckerud, T. RØlland, and L. Arnberg, "Dendrite coherency during equiaxed solidification in binary aluminum alloys," *Metallurgical and Materials Transactions A*, vol. 26, pp. 965-970, 1995.
- [4] G.K. Sigworth and T. A. Kuhn, "Grain Refinement of Aluminum Casting Alloys," in *ASM Handbook*, 9th ed. vol. 15: ASM International, 2008, pp. 255-262.
- [5] E.F.Emley, in *Principles of Magnesium Technology* Oxford, United Kingdom: Pergamon Press, 1966, pp. 126-156, 254-260.
- [6] D. V. Neff, "Nonferrous Molten Metal Processes," in *ASM Handbook*, 9th ed. vol. 15: ASM International, 2008, pp. 477-478.
- [7] M. Johnsson, L. Backerud, and G. Sigworth, "Study of the mechanism of grain refinement of aluminum after additions of Ti- and B-containing master alloys," *Metallurgical and Materials Transactions A*, vol. 24, pp. 481-491, 1993.
- [8] J. Cissé, G. F. Bolling, and H. W. Kerr, "Crystallographic orientations between aluminum grown from the melt and various titanium compounds," *Journal of Crystal Growth*, vol. 13-14, pp. 777-781, 1972.

- [9] G. Jones and J. Pearson, "Factors affecting the grain-refinement of aluminum using titanium and boron additives," *Metallurgical and Materials Transactions B*, vol. 7, pp. 223-234, 1976.
- [10] P. S. Mohanty and J. E. Gruzleski, "Mechanism of grain refinement in aluminium," *Acta Metallurgica et Materialia*, vol. 43, pp. 2001-2012, 1995.
- [11] M. Easton and D. StJohn, "Grain refinement of aluminum alloys: Part I. the nucleant and solute paradigms—a review of the literature," *Metallurgical and Materials Transactions A*, vol. 30, pp. 1613-1623, 1999.
- [12] Reed-Hill R.E. and R. Abbaschian, "Physical Metallurgy Principles," 3rd ed Boston United States: PWS Publishing Co., 1992, p. 496.
- [13] D. Turnbull, "Theory of catalysis of nucleation by surface patches," *Acta Metallurgica*, vol. 1, pp. 8-14, 1953.
- [14] B. E. Sundquist, "On "Nucleation catalysis in supercooled liquid tin"," *Acta Metallurgica*, vol. 11, pp. 630-632, 1963.
- [15] B. Cantor, "Heterogeneous nucleation and adsorption," *Philosophical Transactions of the Royal Society of London. Series A: Mathematical, Physical and Engineering Sciences*, vol. 361, pp. 409-417, March 15, 2003 2003.
- [16] I. Maxwell and A. Hellawell, "A simple model for grain refinement during solidification," *Acta Metallurgica*, vol. 23, pp. 229-237, 1975.
- [17] D. Turnbull, "Kinetics of Solidification of Supercooled Liquid Mercury Droplets," *The Journal of Chemical Physics*, vol. 20, pp. 411-424, 1952.
- [18] A. L. Greer, A. M. Bunn, A. Tronche, P. V. Evans, and D. J. Bristow, "Modelling of inoculation of metallic melts: application to grain refinement of aluminium by Al-Ti-B," *Acta Materialia*, vol. 48, pp. 2823-2835, 2000.
- [19] M. A. Easton and D. H. StJohn, "A model of grain refinement incorporating alloy constitution and potency of heterogeneous nucleant particles," *Acta Materialia*, vol. 49, pp. 1867-1878, 2001.

- [20] M. C. Flemings, *Solidification Processing* New York, McGraw-Hill [1974].
- [21] Y. Lee, A. Dahle, and D. StJohn, "The role of solute in grain refinement of magnesium," *Metallurgical and Materials Transactions A*, vol. 31, pp. 2895-2906, 2000.
- [22] D. StJohn, M. Qian, M. Easton, P. Cao, and Z. Hildebrand, "Grain refinement of magnesium alloys," *Metallurgical and Materials Transactions A*, vol. 36, pp. 1669-1679, 2005.
- [23] M. Qian and A. Das, "Grain refinement of magnesium alloys by zirconium: Formation of equiaxed grains," *Scripta Materialia*, vol. 54, pp. 881-886, 2006.
- [24] Q. Ma, D. H. StJohn, and M. T. Frost, "Characteristic zirconium-rich coring structures in Mg-Zr alloys," *Scripta Materialia*, vol. 46, pp. 649-654, 2002.
- [25] M. Qian, D. H. StJohn, and M. T. Frost, "Heterogeneous nuclei size in magnesium-zirconium alloys," *Scripta Materialia*, vol. 50, pp. 1115-1119, 2004.
- [26] M. Qian, L. Zheng, D. Graham, M. T. Frost, and D. H. StJohn, "Settling of undissolved zirconium particles in pure magnesium melts," *Journal of Light Metals*, vol. 1, pp. 157-165, 2001.
- [27] H. Okamoto, "Mg-Zr (Magnesium-Zirconium)," *Journal of Phase Equilibria*, vol. 23, pp. 198-199, 2002.
- [28] M. Härmäläinen and K. Zeng, "Thermodynamic evaluation of the Mg-Zr system," *Calphad*, vol. 22, pp. 375-380, 1998.
- [29] M. Qian, D. H. StJohn, and M. T. Frost, "Effect of soluble and insoluble zirconium on the grain refinement of magnesium alloys," *Material Science Forum*, vol. 419-422, pp. 593-598, 2002.
- [30] M. Qian, D. H. StJohn, and M. T. Frost, "Zirconium alloying and grain refinement of magnesium alloys," in *Magnesium Technology 2003*, San Diego, California, USA, 2003, pp. 209-214.

- [31] M. Qian, D. H. StJohn, and M. T. Frost, "A new zirconium-rich master alloy for the grain refinement of magnesium alloys," in *Magnesium: Proceedings of the 6th International conference magnesium alloys and their applications*, 2003, pp. 706-712.
- [32] M. Qian, D. H. StJohn, M. T. Frost, and R. M. Barnett, "Grain refinement of pure magnesium using rolled zirmax master alloy (Mg-33.3ZR)," in *Magnesium Technology 2003*, San Diego, California, USA, 2003, pp. 215-220.
- [33] P. Cao, M. Qian, D. H. StJohn, and M. T. Frost, "Uptake of iron and its effect on grain refinement of pure magnesium by zirconium," *Materials Science and Technology*, vol. 20, pp. 585-592, 2004.
- [34] "Multicomponent phase diagram calculations," in *Pandat 5.0 Madison WI USA: Computherm LLC*.
- [35] S. Yi, I. Schestakow, and S. Zaeferrer, "Twinning-related microstructural evolution during hot rolling and subsequent annealing of pure magnesium," *Materials Science and Engineering: A*, vol. 516, pp. 58-64, 2009.
- [36] A. L. Greer, "Grain Refinement of Alloys by Inoculation of Melts," *Philosophical Transactions: Mathematical, Physical and Engineering Sciences*, vol. 361, pp. 479-495, 2003.
- [37] P. Schumacher and A. L. Greer, "Studies of the action of the grain refined particles in aluminum alloys," *TMS (The Minerals, Metals & Materials Society) Light Metal*, pp. 869-877, 1995.
- [38] I. Naglic, A. Smolej, and M. Dobersek, "TEM analysis of the TiC particles in aluminium containing AlTi3C0.15 grain refiner," *Metallic Materials*, vol. 45, pp. 293-299, 2007.
- [39] C. D. Mayes, D. G. McCartney, and G. J. Tatlock, "Observations on the microstructure and performance of an Al---Ti---C grain-refining master alloy," *Materials Science and Engineering: A*, vol. 188, pp. 283-290, 1994.
- [40] M. Qian and D. H. Stjohn, "Grain nucleation and formation in MgZr alloys," *International Journal of Cast Metals Research*, vol. 22, pp. 256-259, 2009.
- [41] M. Treilleux and G. Chassagne, "Orientation relationship and structure of lithium precipitates in MgO single crystals," *J. Physique Lett.*, vol. 40, pp. 283-286, 1979.

- [42] B. Bramfitt, "The effect of carbide and nitride additions on the heterogeneous nucleation behavior of liquid iron," *Metallurgical and Materials Transactions B*, vol. 1, pp. 1987-1995, 1970.
- [43] D. G. McCartney, "Grain refining of aluminium and its alloys using inoculants," *International Materials Reviews*, vol. 34, pp. 247-260, 1989.
- [44] P. Cooper, "Developments in the grain refinement of foundry alloys " *Foundry Trade Journal*, vol. 179, pp. 48-49, March, 2005.
- [45] T. E. Quested and A. L. Greer, "The effect of the size distribution of inoculant particles on as-cast grain size in aluminium alloys," *Acta Materialia*, vol. 52, pp. 3859-3868, 2004.
- [46] I. Davies, J. Dennis, and A. Hellawell, "The nucleation of aluminum grains in alloys of aluminum with titanium and boron," *Metallurgical and Materials Transactions B*, vol. 1, pp. 275-280, 1970.
- [47] L. Lu, A. K. Dahle, and D. H. StJohn, "Grain refinement efficiency and mechanism of aluminium carbide in Mg-Al alloys," *Scripta Materialia*, vol. 53, pp. 517-522, 2005.
- [48] Y. Liu, X. Liu, and B. Xiufang, "Grain refinement of Mg-Al alloys with Al<sub>4</sub>C<sub>3</sub>-SiC/Al master alloy," *Materials Letters*, vol. 58, pp. 1282-1287, 2004.
- [49] M. A. Easton, A. Schiffl, J.-Y. Yao, and H. Kaufmann, "Grain refinement of Mg-Al(-Mn) alloys by SiC additions," *Scripta Materialia*, vol. 55, pp. 379-382, 2006.
- [50] R. Günther, C. Hartig, and R. Bormann, "Grain refinement of AZ31 by (SiC)P: Theoretical calculation and experiment," *Acta Materialia*, vol. 54, pp. 5591-5597, 2006.
- [51] L. Lu, A. K. Dahle, and D. H. StJohn, "Heterogeneous nucleation of Mg-Al alloys," *Scripta Materialia*, vol. 54, pp. 2197-2201, 2006.
- [52] M. Qian and P. Cao, "Discussions on grain refinement of magnesium alloys by carbon inoculation," *Scripta Materialia*, vol. 52, pp. 415-419, 2005.
- [53] T. Motegi, "Grain-refining mechanisms of superheat-treatment of and carbon addition to Mg-Al-Zn alloys," *Materials Science and Engineering: A*, vol. 413-414, pp. 408-411, 2005.

- [54] R. H. Gunther, Ch. Anopuo, O. Hort, N. Bormann, R., "The Role of Solutes for Grain Refinement by (SiC) P : Experiment and Theoretical Calculation " *TMS (The Minerals, Metals & Materials Society) Magnesium Technology*, pp. 95-99, 2008.
- [55] M. Qian, "Heterogeneous nucleation on potent spherical substrates during solidification," *Acta Materialia*, vol. 55, pp. 943-953, 2007.
- [56] D. H. StJohn, P. Cao, M. Qian, and M. A. Easton, "A New Analytical Approach to Reveal the Mechanisms of Grain Refinement," *Advanced Engineering Materials*, vol. 9, pp. 739-746, 2007.
- [57] D. H. Stjohn, M. A. Easton, P. Cao, and M. Qian, "New approach to analysis of grain refinement," *International Journal of Cast Metals Research*, vol. 20, pp. 131-135, 2007.
- [58] M. Easton and D. StJohn, "An analysis of the relationship between grain size, solute content, and the potency and number density of nucleant particles," *Metallurgical and Materials Transactions A*, vol. 36, pp. 1911-1920, 2005.
- [59] V. M. Segal, K. T. Hartwig, and R. E. Goforth, "In situ composites processed by simple shear," *Materials Science and Engineering A*, vol. 224, pp. 107-115, 1997.
- [60] ASTM Standard E112-96, "Standard Test Methods for Determining Average Grain Size," West Conshohocken, PA: ASTM International, , 2003.

## APPENDIX

### A.1. Grinding and Polishing Procedures for Pure Magnesium and its Alloys

Grinding: Primary grinding was performed using SiC # 320 grit as the abrasive surface and distilled water as the grinding media until the surface become smooth and flat. After the primary grinding step, the surface was rinsed with isopropanol for 5 s. Next, the metallographic specimens were cleaned with an ultrasonic agitator and isopropanol for 2 min and dried with hot air. Final grinding was carried out with a water based diamond suspension (DiaPro 9  $\mu\text{m}$  particle size) and MD-Largo cloth for 3 min in a semi-automatic polisher (Struer<sup>®</sup> Tegra Poll semi-automatic polishing system). The specimen holder plate (applied force 20 kN for each specimen) and the magnetic platen were rotated at same direction (complementary rotation at 150 rpm). After final grinding the specimens were rinsed with hot water followed by isopropanol for 5 s. The specimens were cleaned using an ultrasonic agitator for 2 min in isopropanol media and dried with hot air.

Polishing: Final polishing was carried out using a water based diamond suspension (DiaPRo 3  $\mu\text{m}$  particle size) and MD-Mol cloth for 5 min. The specimen holder plate (applied force 20 kN for each specimen) and the magnetic platen were rotated at same direction (complementary rotation at 150 rpm). Final polishing was performed using 0.04  $\mu\text{m}$  particle size colloidal silica suspension and MD Mol cloth for 1 min. After final polishing the specimens were

rinsed with hot water followed by isopropanol for 5 s. The specimens were cleaned using an ultrasonic agitator for 2 min in isopropanol media and dried with hot air.

Etching: Specimens were etched with standard acetic-picral etchant (5 mL acetic acid, 6 g picric acid, 10 mL water, and 100mL ethanol) until a brown film appeared on the surface and then rinsed with water and dried with hot air.

## **A.2. Grain Size Measurement Method Following ASTM Standard E112-96**

Grain size was determined following the standard procedures outlined in ASTM standard E112-96 [60]. Three concentric circles with diameters of 79.58 mm, 53.05 mm, and 26.53 mm, with a total circumference of 500 mm, were drawn on each optical micrograph printed out on letter-size paper (8½ by 11 inches). The actual magnification of the photomicrograph was adjusted by measuring the length of the micron marker. A set of three concentric circles were drawn at the center of the micrographs captured 2 mm from bottom of the hockey puck specimens. Grain boundary intercepts (P) were counted as one point, triple-point intersections were counted as 1½ points, and tangent hits were counted as one-half point. The intercept values were calculated as follows:

$$P_L = \frac{P}{L_T/M}$$

Where  $P_L$  = number of grain boundary intercepts/length

$L_T$  = total line length (500 mm)

$M$  = magnification

The mean intercept length (mean lineal intercept)  $\bar{L}_3$  was calculated from the following relationship

$$\bar{L}_3 = \frac{1}{P_L}$$

In general, while measuring grain size by the lineal intercept method it is always checked that the total number of grain boundary intercepts fall between 70 and 140. Most of our measurements were taken at 25x magnification images where the total numbers of grain boundary intercepts were in the range of 60-70 but in a few cases 3 x 3 images were stitched together at 25x magnifications if the total number of intercepts were very small.